Department of Physics and Astronomy
Heidelberg University

Master thesis
in Physics
submitted by

Erik Walendy

born in Mannheim, Germany

2024

Thermodynamic and Magnetic Studies on the van-der-Waals Ferromagnet Fe_3GeTe_2 and the Rare-Earth Orthochromite $SmCrO_3$

This Master thesis has been carried out by Erik Samuel Walendy
at the
Kirchhoff-Institut für Physik in Heidelberg
under the supervision of
Prof. Dr. Rüdiger Klingeler
and
Prof. Dr. Christian Enss
Kirchhoff-Institut für Physik in Heidelberg

Thermodynamic and Magnetic Studies on the van-der-Waals Ferromagnet Fe_3GeTe_2 and the Rare-Earth Orthochromite $SmCrO_3$

This work presents thermodynamic and magnetic studies on the quasi-2D van-der-Waals ferromagnet Fe_3GeTe_2 and the rare earth orthochromite $SmCrO_3$. For Fe_3GeTe_2 dilatometric measurements feature a distinct anomaly in thermal expansion along the c axis, which is associated with the ferromagnetic phase transition, implying a significant magnetoelastic coupling. At low fields, magnetostriction measurements show a rise caused by the alignment of magnetic moments with the magnetic field and a hysteresis at higher fields of unknown origin. The entropy change in $SmCrO_3$ associated to the spin rotation transition in zero field is determined to $47(6)\,\mathrm{mJ\,mol^{-1}\,K^{-1}}$ from heat capacity measurements, which agrees to the thermodynamic analysis of the phase boundaries for $B \parallel c$. A Schottky anomaly, signalling the presence of an internal magnetic field at the Sm^{3+}-sites, is observed for $T < T_{\mathrm{SRT}}$. It disappears above $T \geq T_{\mathrm{SRT}}$, suggesting a change of the internal field by the rotation of the moments of the Cr^{3+}-ions. Furthermore, the magnetic phase diagram from [1] is continued up to magnetic fields of 14 T.

Thermodynamische und magnetische Untersuchungen des Van-der-Waals Ferromagneten Fe_3GeTe_2 und des Seltenerd-Orthochromit $SmCrO_3$

In dieser Arbeit werden thermodynamische und magnetische Untersuchungen des quasi-2D Van-der-Waals Ferromagneten Fe_3GeTe_2 und des Seltenerd-Orthochromit $SmCrO_3$ diskutiert. Dilatometrische Messungen an Fe_3GeTe_2 entlang der c Achse zeigen eine deutliche Anomalie in der thermischen Ausdehnung, welche mit einem ferromagnetischen Phasenübergang assoziiert wird. Die Anwesenheit dieser Anomalie deutet auf eine starke magnetoelastische Kopplung hin. Bei tiefen Magnetfeldern ist ein Anstieg in der Magnetostriktion sichtbar, welcher durch das Ausrichten der magnetischen Momente entlang des Magnetfeldes verursacht wird. Zusätzlich zeigen die Messungen bei hohen Magnetfeldern eine Hysterese mit unbekanntem Ursprung. Mit Hilfe von Wärmekapazitätsmessungen wurde eine Entropieänderung von $47(6)\,\mathrm{mJ\,mol^{-1}\,K^{-1}}$ in $SmCrO_3$ ermittelt, welche dem Spin-Rotations-Übergang im Nullfeld zugeordnet wird. Dieses Ergebnis stimmt mit den Ergebnissen thermodynamischer Untersuchungen der Phasengrenzen von $B \parallel c$ überein. Des Weiteren wurde eine Schottky Anomalie für $T < T_{\mathrm{SRT}}$ gefunden. Diese deutet auf ein internes Magnetfeld an den Sm^{3+}-Gitterpositionen hin. Die Schottky Anomalie ist oberhalb von $T \geq T_{\mathrm{SRT}}$ nicht beobachtbar, was durch eine Änderung dieses internen Magnetfeldes durch die Rotation der magnetischen Momente der Cr^{3+}-Ionen erklärt werden kann. Darüber hinaus wurde das magnetische Phasendiagramm von [1] um Messungen bei Magnetfeldern bis zu 14 T erweitert.

Contents

1 Introduction **1**

2 Theoretical Background **3**
2.1 Thermodynamic Potential and Response Functions 3
2.2 Thermodynamic Phase Transitions 4
2.3 Clausius-Clapeyron Equation 6
2.4 Thermal expansion and Grüneisen Scaling 6
2.5 Heat Capacity 8
2.5.1 Lattice Specific Heat 8
2.5.2 Schottky Anomaly 9

3 Experimental Methods **11**
3.1 Heat Capacity 11
3.1.1 Measuring Heat Capacity on $SmCrO_3$ 14
3.2 High-Resolution Capacitance Dilatometry 19
3.2.1 Cell Effect 21
3.3 Magnetisation Measurements 26

4 Dilatometric Measurements on Fe_3GeTe_2 **29**
4.1 Thermal Expansion Measurements 30
4.2 Magnetostriction Measurements 33

5 $SmCrO_3$ **37**
5.1 Introduction 37
5.1.1 Entropy Changes at T_{SRT} 41
5.2 Heat Capacity Measurements 45
5.2.1 Heat Capacity at $B = 0\,T$ 45
5.2.2 Heat Capacity at $B \neq 0\,T$ 50
5.3 Magnetic Phase Diagrams 56

6 Conclusions **61**

Bibliography **63**

Chapter 1

Introduction

"A whole new World" as Aladdin sings in the same named musical [2] opens up when exploring strongly correlated electron systems. These systems show a "hundred thousand things to see" such as superconductivity, spin liquids or two dimensional ferromagnetism which are "[s]hining, shimmering, splendid".

The first new world explored in this work is that of Fe_3GeTe_2. Its "new fantastic point of view" is a ferromagnetic long range order down to the monolayer limit [3]. Magnetic two dimensional order is not expected when the system is isotropic as shown by the Mermin-Wagner-Berezinskii theorem [4]. However, it was proven that a single layer of Fe_3GeTe_2 can order, as the material hosts magnetocrystalline anisotropy [5]. Exploring the world of two dimensional magnetism has "new horizons to pursue", which may show new exotic phases such as quantum spin liquids [6]. The method used for studying Fe_3GeTe_2 in this work, is high resolution capacitance dilatometry which allows to measure length changes of macroscopic samples down to 1 pm [7] and therefore deepen the understanding of the interplay between lattice and magnetism [8].

The second new world explored within this work is $SmCrO_3$. $SmCrO_3$ hosts a sublattice of the magnetic moments of the samarium and a chromium that interact with each other. This interaction gives rise to a rich phase diagram [9, 10] and a range of phenomena such as a spin reorientation transition [11]. The order of the spin reorientation transition is not "crystal clear" [12, 13, 14], showing the need for further research. Moreover, $SmCrO_3$ hosts spin phonon coupling and ferroelectric order [15, 16]. Investigations using magnetization and heat capacity measurements are conducted in order to further investigate the spin rotation transition and expand the phase diagram.

The structure of this thesis is as follows: Chapter 2 gives a short overview of the theoretical concepts used in this work. Chapter 3 briefly describes the technique of heat capacity, high-resolution capacitance dilatometry and magnetization measurements and specifies the setups used. This is followed by the thermal expansion and magnetostriction measurements on Fe_3GeTe_2, presented in chapter 4. Chapter

5 shows heat capacity measurements on $SmCrO_3$ and the entropy change in the spin rotation transition is calculated and compared to the entropy change calculated using the Clausius-Clapeyron equation. Magnetization measurements allowed for expansion of the phase diagram up to 14 T. In chapter 6 this work is concluded and the results are summarized.

Chapter 2

Theoretical Background

This chapter introduces the theoretical models and methods used in this work. The derivation and precise explanation of the formulas and concepts is omitted. For a more detailed insight into them it is referred to literature. For this introduction the following resources were used [17, 18, 19, 20, 21].

2.1 Thermodynamic Potential and Response Functions

The thermodynamic potential describes the equilibrium of a system using a certain set of variables. Assuming a constant number of particles in a solid the total differential of the Gibbs free energy G can be written as:

$$dG = Vdp - SdT - MVdH \tag{2.1}$$

where V is the volume of the solid, p is the pressure it is subjected to, S is the entropie, T is its temperature, $M = {}^{m}/_{V}$ is its Volume magnetisation with m the magnetisation and H the magnetic field strength[1]. By calculating the second derivative of dG with respect to the state variables p, T, H the response functions are obtained. They are shown in table 2.1 and describe the change of the system if one of the variables describing the environment is changed.

The thermal expansion coefficient β and the magnetostriction coefficient Λ describe the volume change of the solid when temperature or applied magnetic field are changed respectively. In this work not the volume change is measured but the length change along an axis making the thermal expansion coefficient a vector. Furthermore the magnetic field has a direction from which it is applied making the

[1] In latter chapters both magnetic field and magnetic field strength are denoted with B

Response function	Symbol	Definition	Gibbs presentation
Magnetic Susceptibility	χ	$\frac{1}{V}\frac{\partial(MV)}{\partial H}\big\vert_p, T$	$-\frac{1}{V}\frac{\partial^2 G}{\partial H^2}\vert_{p,T}$
Specific heat capacity	c_p	$T\frac{\partial S}{\partial T}\vert_{p,H}$	$-T^2\frac{\partial^2 G}{\partial^2 T}\vert_{p,H}$
Thermal expansion coefficient	β	$\frac{1}{V}\frac{\partial V}{\partial T}\vert_H$	$-\frac{1}{V}\frac{\partial^2 G}{\partial p \partial T}\vert_H$
Magneostriction coefficient	Λ	$\frac{1}{V}\frac{\partial V}{\partial H}\vert_T$	$-\frac{1}{V}\frac{\partial^2 G}{\partial p \partial H}\vert_T$

Table 2.1: Thermodynamic response function their symbol, definition and Gibbs representation.

uniaxiale magnetostriction coefficient a Tensor:

$$\alpha_i = \frac{1}{L_i}\frac{\partial L_i}{\partial T}\bigg|_H \tag{2.2}$$

$$\lambda_{ij} = \frac{1}{L_i}\frac{\partial L_i}{\partial H_i}\bigg|_T \tag{2.3}$$

where α_i is the uniaxial thermal expansion coefficient measured along the crystallographic direction i and λ_{ij} is the entry ij in the uniaxial magnetostriction coefficient measured along the crystallographic direction i with magnetic field applied parallel the direction j. In this work the magnetic field is applied parallel to the axis along which the length change is measured: $i = j$. Thus only one index will be written in the case of this work.

2.2 Thermodynamic Phase Transitions

A change of the intensive variables can lead to a abrupt change of the macroscopic properties of a thermodynamic system [20]. An example for a phase transition is water freezing or the emergence of long range order in a magnet.

Phase transitions can be categorized by the Ehrenfest classification. It classifies them by order n, where a phase transition is of order n if a n^{th} derivative of the thermodynamic potential exists which is discontinuous where as all derivatives of lower order are continuous [17].

In Fig. 2.1 the Gibbs free energy and one of its first and second derivatives, the volume and heat capacity respectively are shown in dependency of temperature. In (a) and (b) a first and second order phase transition occur respectively at a temperature indicated by the dashed line. The first order phase transition causes a jump in the volume and a δ like anomaly [17]. The second order phase transition causes a kink in the volume and a jump in the heat capacity.

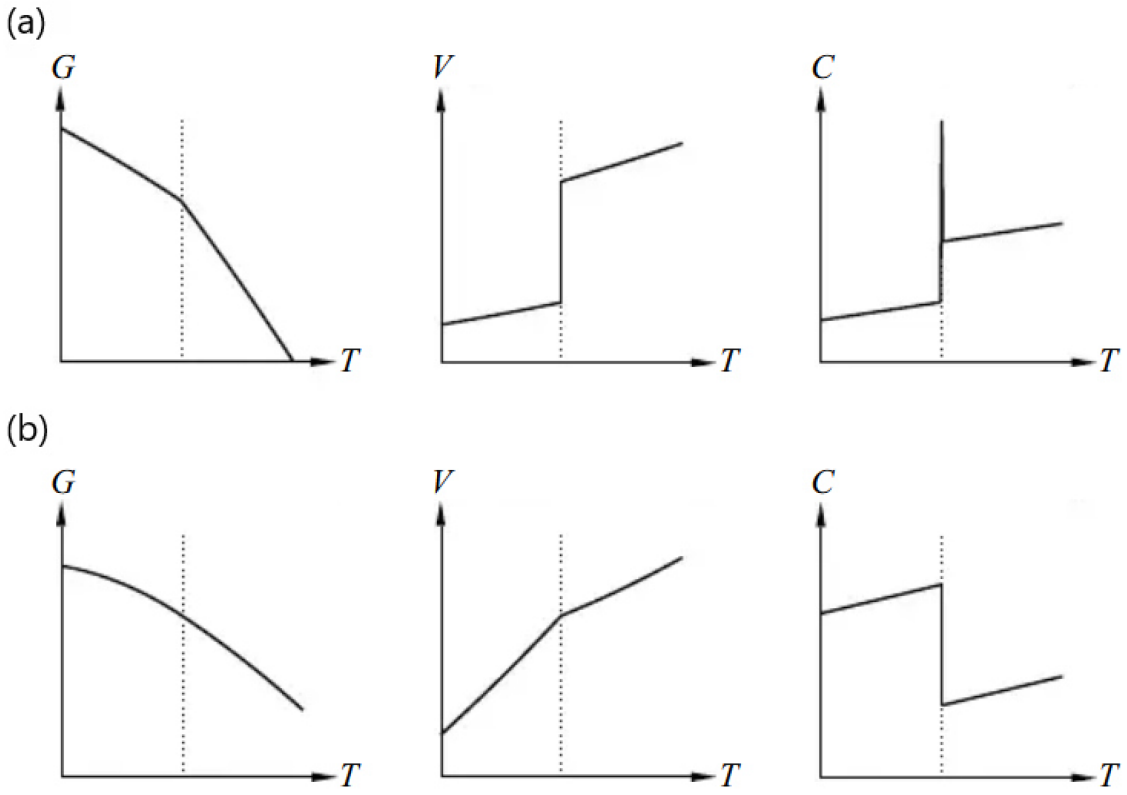


Figure 2.1: Gibbs free energy G, one of it's first derivative the Volume V and one of its second derivatives the heat capacity C. The dashed line marks the temperature of a first (a) and second (b) order phase transition. From [17].

2.3 Clausius-Clapeyron Equation

The Clausius-Clapeyron equation can be derived from the thermodynamic potential and the continuity of the Gibbs free energy [22]. Due to the continuity of Gibbs free energy it must be equal at the phase transition in both phases one and two:

$$dG_1 = V_1 dp - S_1 dT - M_1 V_1 dH = V_2 dp - S_2 dT - M_2 V_2 dH = dG_2. \tag{2.4}$$

Assuming a constant pressure ($dp = 0$) the equation can be transformed to:

$$\Delta S = -\Delta m \cdot \frac{dH}{dT} \tag{2.5}$$

giving the Clausius-Clapeyron equation where ΔS is the jump in entropy, Δm is the jump of magnetisation and $^{dH}/_{dT}$ is the temperature derivative of the magnetic field strength. [22]

2.4 Thermal expansion and Grüneisen Scaling

This introduction is additionally to the sources at the beginning of the chapter based on [23]. In a solid an interplay of repulsive and attractive forces exist between the atoms [23]. The result is a potential depending on the distance between the atoms. If the energy of the solid and the potential is known the equilibrium position can be calculated. At finite temperatures the atoms oscillate around the equilibrium position. The potential and the equilibrium position with growing energy are shown in Fig. 2.2. It shows the potential energy of an atom in dependence of the distance between the atom and a neighboring atom for the harmonic (blue) and anharmonic (red) case. Furthermore, it shows the equilibrium position of the atom for different energies if the potential is harmonic or anharmonic. For the equilibrium position to change with temperature one needs to include anharmonic terms which are of the order three or larger. Including these leads to an equilibrium position at larger distances between the atoms for states with higher energy. This simple model can only explain longitudinal vibrations. As a transversal vibration leads to a length change orthogonal to the propagation vector of the vibration.

With the definition of the uniaxial thermal expansion coefficient in eq. 2.3 and a anharmonic potential the uni axial thermal expansion coefficient can be calculated using thermodynamic relations:

$$\alpha = \frac{1}{L}\frac{\partial L}{\partial T}\bigg|_p = -\frac{\kappa}{3}\sum_{\boldsymbol{q},s}\left(\frac{\partial \hbar\omega_s(\boldsymbol{q})}{\partial V}\frac{\partial n_s(\boldsymbol{q})}{\partial T}\right) \tag{2.6}$$

where κ is the compressibility, ω_s the vibration frequency and $n_s(\boldsymbol{q})$ is the occupation probability of the phononic state with momentum vector $\boldsymbol{q}$ of the branch s.

The heat capacity of a phonon of the branch s is given by:

$$c_{p,s}(\boldsymbol{q}) = \frac{\hbar\omega_s(\boldsymbol{q})}{V}\frac{\partial n_s(\boldsymbol{q})}{\partial T}. \tag{2.7}$$

by defining the Grüneisenparameter for a phonon $\boldsymbol{q}$ from the branch s:

$$\gamma_{\boldsymbol{q},s} = -\frac{\partial \ln \omega_s(\boldsymbol{q})}{\partial \ln(V)} \tag{2.8}$$

equation 2.6 can be rewritten as:

$$\alpha = \frac{\kappa}{3} \sum_{\boldsymbol{q},s} c_{p,s}(\boldsymbol{q}) \gamma_{\boldsymbol{q},s}. \tag{2.9}$$

This equation shows that the thermal expansion coefficient can be put into relation to the heat capacity. If one dominant energy scale drives the entropy changes in the system, eq. 2.9 can be simplified to [24]:

$$\alpha = \frac{1}{3} \kappa \gamma c_p. \tag{2.10}$$

This allows to investigate if a single energy scale drives the entropy changes of a system by measuring heat capacity and thermal expansion and examining if their ratio is constant.

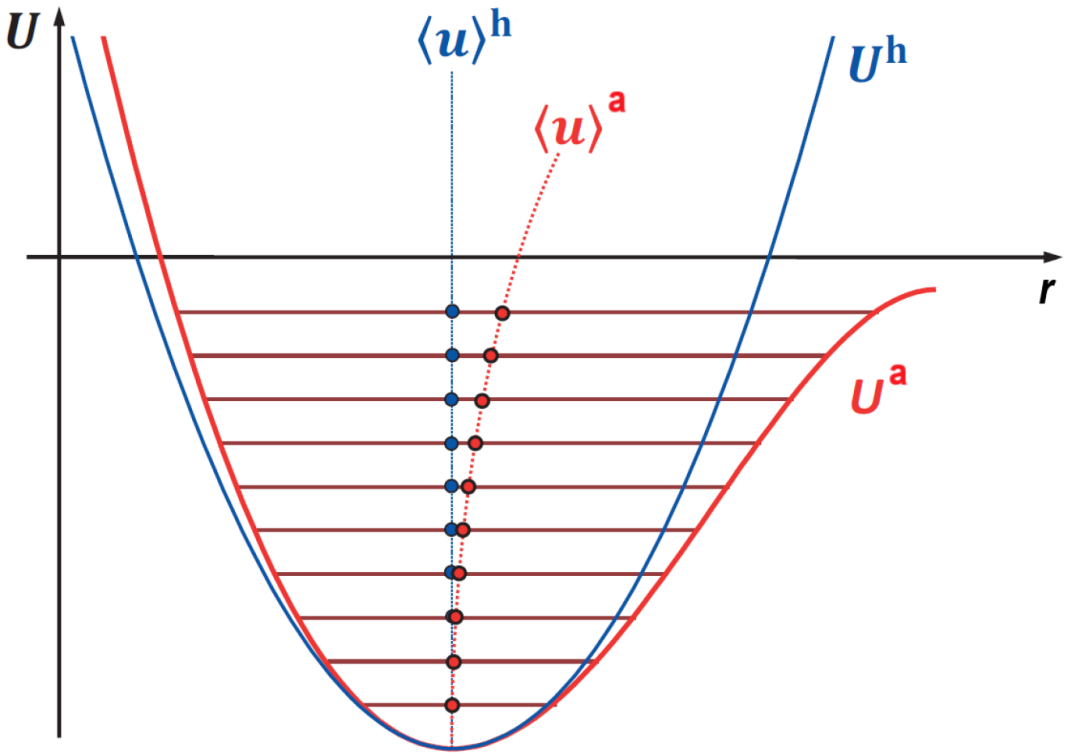


Figure 2.2: Potential energy of an atom in dependence of the distance to a neighboring atom. The blue curve is the harmonic and the red curve the anharmonic case. The equilibrium distance $\langle u \rangle$ of the atom to a neighboring atom is marked for both cases in the corresponding colors. From [23].

2.5 Heat Capacity

This introduction is based on the introduction of [25] combined with the resource [26].

From the definition of heat capacity follows that a change in entropy can be determined from the heat capacity by:

$$\Delta S = \int \frac{c_p}{T}\, dT. \tag{2.11}$$

2.5.1 Lattice Specific Heat

Einstein Model

The Einstein model describes atoms in a lattice which oscillate harmonically with one frequency ω_{E}. In this work it is used to describe optical phonons. Its specific heat is given by:

$$c_{\mathrm{E}} = 3n_{\mathrm{E}}R\left(\frac{\theta_{\mathrm{E}}}{T}\right)^2 \frac{\exp\left(\frac{\theta_{\mathrm{E}}}{T}\right)}{\left(\exp\left(\frac{\theta_{\mathrm{E}}}{T}\right)-1\right)^2} \tag{2.12}$$

where R is the molar gas constant, $\theta_{\mathrm{E}} = {}^{\hbar\omega_{\mathrm{E}}}/_{k_{\mathrm{B}}}$ is the Einstein temperature and n_{E} is the number of atoms per unit cell. The model describes the lattice specific heat well for high temperatures at $T \gg \theta_E$, but at low temperatures ($T \ll \theta_E$) its specific heat capacity behaves exponential which deviates from the observed heat capacity of a lattice.

Debye Model

The Debye model assumes a linear dispersion relation $\omega(q) = v_s q$ and a density of states $D(\omega)$ of zero above, the Debye frequency ω_{D}. From this follows, that the density of states is given by:

$$D(\omega) = \begin{cases} \frac{3n_D\omega^2}{\omega_{\mathrm{D}}^3} & \omega \leq \omega_{\mathrm{D}} \\ 0 & \omega \geq \omega_{\mathrm{D}} \end{cases} \tag{2.13}$$

where n_{D} is the number of atoms per unit cell and ω is the frequency. With the energy relation of a harmonic oscillator the heat capacity c_{D} follows as:

$$c_{\mathrm{D}} = 9Rn_{\mathrm{D}}x_{\mathrm{D}}^{-3}\int_0^{x_{\mathrm{D}}} \frac{x^4\exp(x)}{(\exp(x)-1)^2}\, dx \tag{2.14}$$

where $x = {}^{\theta_{\mathrm{D}}}/_T = {}^{\hbar\omega_{\mathrm{D}}}/_{k_{\mathrm{B}}T}$ with θ_{D} the Debye temperature and $\hbar$ the reduced Plank constant. The Debye model is used to describe the contribution of accoustic phonons to the heat capacity.

To describe the contribution of a lattice with several atoms per unit cell to the specific heat a model that contains several Einstein and Debye models that are added up is used.

The materials in this work have lattices with several atoms per unit cell. Thus it is possible that they have several acoustic and optic phonon modes. To describe the heat capacity of the lattice a model containing a sum of several Einstein and Debye models is used. The Debye models describe the acoustic and the Einstein models describe the optical phonons.

2.5.2 Schottky Anomaly

When a System has two discrete energy levels seperated by the energy Δ a broad anomaly shows in the specific heat which is called a Schottky peak. Its cause is an increase in entropy when the thermal energy is large enough such that the higher energy level can be populated. As the heat capacity is the derivative of the entropy the increase in entropy causes a peak in c_p. For a two state system the heat capacity of a Schottky anomaly is given by:

$$c_{\text{Schottky}} = R\left(\frac{\Delta}{k_B T}\right)^2 \frac{\exp\left(\frac{\Delta}{k_\text{B} T}\right)}{\left(1+\exp\left(\frac{\Delta}{k_\text{B} T}\right)\right)^2} \tag{2.15}$$

where k_B is the Boltzmann constant. The maximum of the Schottky anomaly is at approximately $T_M = 0.42\,{}^{\Delta}/_{k_\text{B}}$ [26].

Chapter 3

Experimental Methods

3.1 Heat Capacity

Heat capacity in this work is measured using the heat capacity option of the Physical Properties Measurement System (PPMS) built by Quantum Design (The information given in this chapter is taken from [27]). The PPMS is a cryogenically cooled device accessing temperatures between 1.8 K and 400 K with the heat capacity option installed (50 mK with the dilution refrigerator option). Measurements can be conducted in magnetic fields up to 14 T.

The heart of the heat capacity option is the puck shown in Fig. 3.1 (b). The important components for a basic understanding of a normal measurement operation are explained in the following. The sample is mounted to the sample platform by Apiezon® N-grease[1] to ensure good thermal contact. Connected to the sample platform are a heater and a thermometer in the form of two resistors, that are controlled over two Gold wires. In total there are eight gold wires which establish thermal contact from the sample platform to the puck. In the puck frame is another thermometer. The puck is mechanically and thermally connected to the PPMS through the chuck fingers and 12 hole pins. A thermal radiation shield is put on top of the puck also functioning as a mechanical shield for the sample. To suppress thermal exchange with the surrounding by gas the sample champer is kept below a pressure of 1 mTorr while measuring by a charcoal inset and a sorption pump [28]. Fig. 3.1 (a) shows a sample installed on the puck.

Samples were mounted using a microscope and the PPMS sample mounting station. The sample platform was cleaned carefully using ethanol and a cotton swab and a wooden pick. Then N-grease was applied using a metal tweezer or a wooden pick. To spread the grease on the platform, it was heated using a heat gun at 50 °C for 10 s to decrease its viscosity, the method is adapted from [29]. Background measurements (addendas) at the temperature and fields of the planned coming sample

[1] Apiezon® N-grease was used, as the temperature regime in which investigations were conducted is below 200 K

measurements were performed. The sample was then installed on the sample platform by gently pressing it into the grease until it connected to the platform. Some samples were so small, that handling them with tweezers was impossible. These were installed by taking one side of a tweezer and applying a very small amount of N-grease onto it as a glue to which the sample stuck and then performing the afore mentioned steps.

Fig. 3.2 shows the temperature of the platform during one heat capacity measurement against the time after the heater was turned on. While the heater is on the temperature rises, the decreasing slope is due to more heat energy being lost to the puck with an increasing temperature difference between puck and platform. When the platform temperature has risen up to the programmed temperature the heater is turned of. The temperature then decreases to the puck temperature. Assuming good thermal contact, such that the platform and the sample are at the same temperature T at all times the rising and falling temperatures can each be described by the differential equation [27]:

$$c_{\text{total}} \frac{dT}{dt} = -K_w(T - T_b) + P(t) \tag{3.1}$$

where t is the time and $P(t)$ is the power of the heater which is constant for the temperature rise and 0 when the temperature falls. T_b is the temperature of the puck frame which is constant as its heat capacity is much larger than the heat capacity c_{total} of the platform, the grease and the sample. K_w is the thermal conductance of

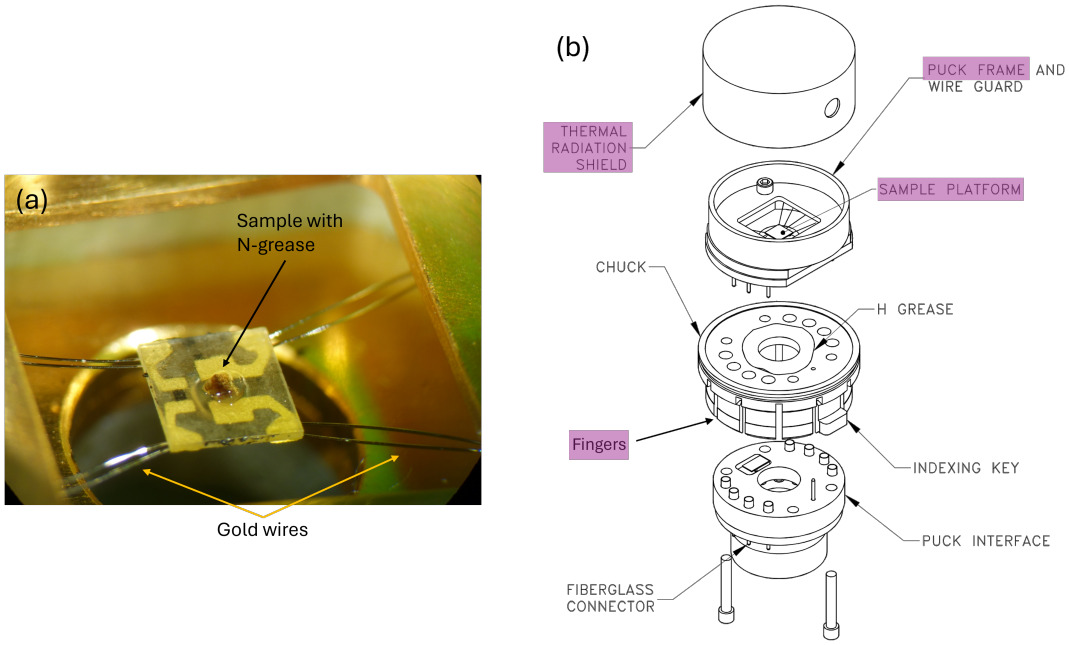


Figure 3.1: **(a)** A sample attached to the platform through a thin layer of N-grease. **(b)** Exploded view of the Puck modified, from [27].

the gold wires. The solution of this model is:

$$T(t) = A \cdot \exp\left(-\frac{t \cdot K_w}{c_{\text{total}}}\right) + T_b + \frac{P(t)}{K_w} \tag{3.2}$$

By fitting the solution to the temperature curves the total heat capacity of the platform, grease and sample can be determined. As the heat capacity of the platform and sample are known from the addenda measurement the heat capacity can be extracted.

When the sample and the platform are not thermally perfectly connected to each other the sample temperature T_{sample} and platform temperature T_{platform} may differ. Then the model in eq. 3.1 cannot be applied. In this case the Two-tau model™ can be used in it the different temperatures lead to a heat flow between sample and platform with a thermal conductance of K_g. The model is described by the equations [27]:

$$c_{\text{platform}} \frac{dT_{\text{platform}}}{dt} = P(t) - K_w\big(T_{\text{platform}}(t) - T_b\big) + K_g\big(T_{\text{sample}}(t) - T_{\text{platform}}(t)\big) \tag{3.3}$$

$$c_{\text{sample}} \frac{dT_{\text{sample}}}{dt} = -K_g\big(T_{\text{sample}}(t) - T_{\text{platform}}(t)\big) \tag{3.4}$$

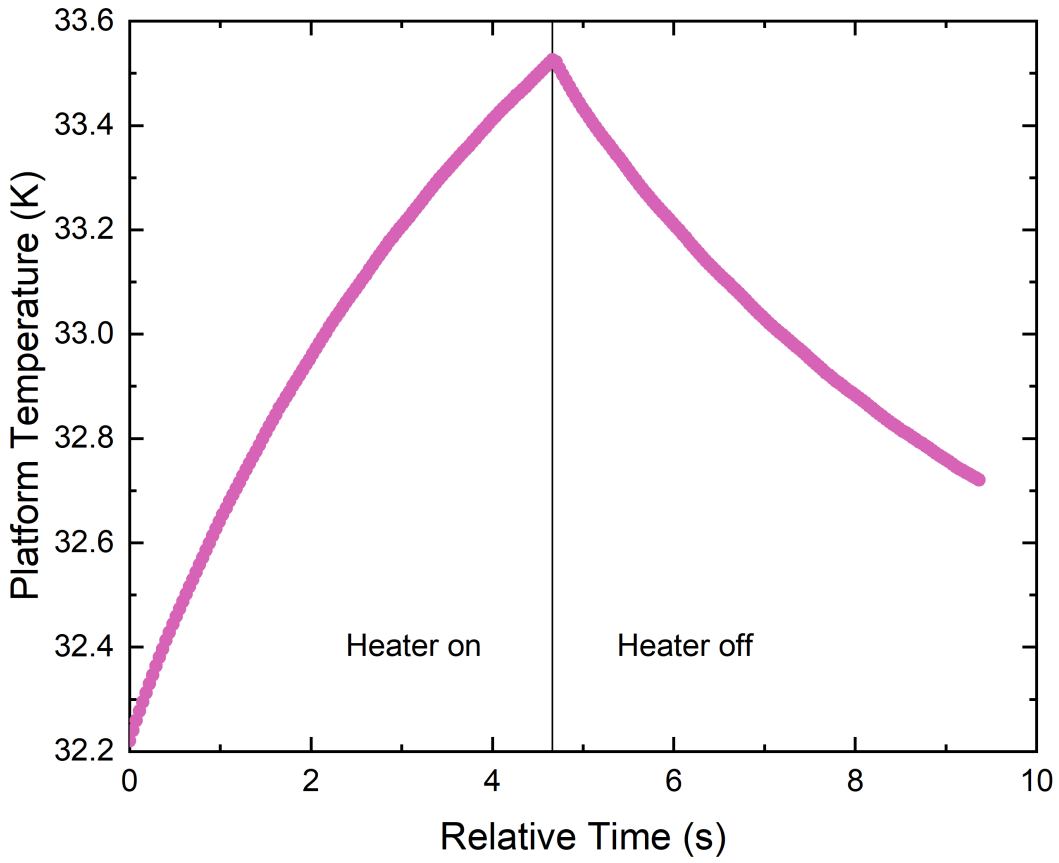


Figure 3.2: Temperature of the platform as a function of time after the heat pulse was applied.

where c_{platform} and c_{sample} are the heat capacities of the platform and sample respectively. The heat capacity of the platform is known by the addenda.

Detecting a first order phase transition by measuring temperature rises and then fitting one of the models can be difficult. As the heat capacity is calculated from a temperature rise it is the heat capacity over a temperature interval and not for a single temperature. A first order phase transition can occur in a very narrow temperature interval that is smaller than a temperature rise. In this case the phase transition is only in one measurement point and the fit of the models won't work, as they assume a constant heat capacity for all temperatures during a temperature rise. A first order transition leads to a kink in the temperature rise curves (Fig. 3.2) [27].

3.1.1 Measuring Heat Capacity on $SmCrO_3$

Heat capacity measurements were conducted on a $SmCrO_3$ sample using the mounting method described in chapter 3.1. The mounted $SmCrO_3$ sample is shown in Fig. 3.3 (a), with the c axis pointing into the picture. When measuring the heat capacity of $SmCrO_3$ starting at low temperatures the sample coupling is at first above the by Quantum Design recommended value of 90% [27, p. 4-15]. With rising temperatures the sample coupling drops below this value around temperatures of 10 to 15 K (see 3.4 (a)). For higher temperatures there are measurements where a sample coupling cannot be determined anymore or it is determined to be 100%. Furthermore the temperature rise curves to which the PPMS fits to determine the heat capacity also show a oscillation with a frequency of the order of 0.6 sec. Remounting the sample several times with varying amounts of grease, did not improve the sample coupling. Different potential causes where investigated:

- Between 1.8 to 10 K the cooling is done with different modes. Therefore measurements starting at higher temperature and with going in temperature down instead of rising temperature were performed. [2]

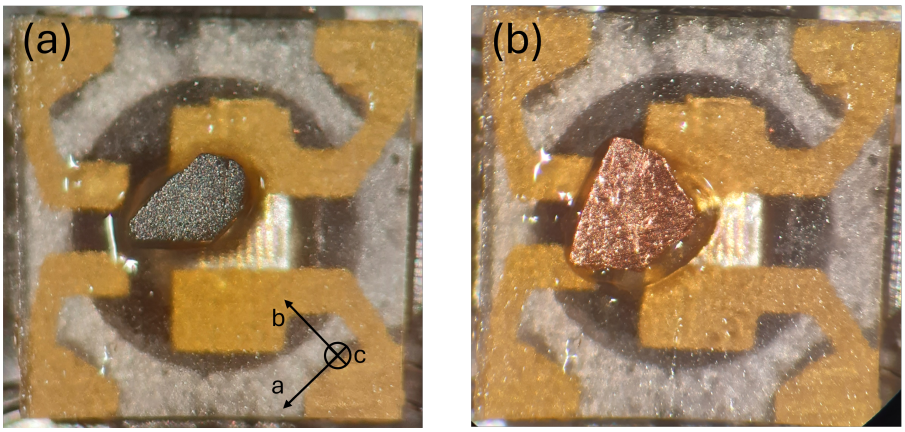


Figure 3.3: Platform of the heat capacity puck with **(a)** the $SmCrO_3$ and **(b)** the Copper sample. In (a) the crystallographic orientation is noted.

[2] This also eliminated the theory that helium which condenses on the calorimeter or in the

- The roughness of the surface of the sample seemed to be large. The sample was polished, which decreased the mass from 2.41 mg to 0.69 mg.
- A small temperature rise could make fitting difficult for a small sample. Therefore the temperature rise was increased from 0.5% up to 4%.
- The thermal contact between the fingers of the Puck and the PPMS or another characteristic of the Puck may have changed over time. To take these factors into account the Puck fingers were spread using the spreading tool and the Puck was recalibrated.

These measures did not improve the sample coupling. The problem is caused by the small heat capacity of the sample, as Quantum Design specifies that the sample mass should be in the range from 1 to 200 mg [27, p. 1-2]. Accordingly the sample mass of 2.41 mg is on the lower limit of the calorimeter capability and this became even worse after polishing the sample and reducing its mass to 0.69 mg, which directly implies a small heat capacity. To investigate this a Copper piece was ground down to 0.74 mg and its heat capacity was measured, the mounted sample is shown in Fig. 3.3 (b). The sample coupling of $SmCrO_3$ and Copper against temperature can be seen in Fig. 3.4 (a). Unlike the sample coupling of $SmCrO_3$ the coupling of Copper at low temperatures is below 90%. Similar to the sample coupling of $SmCrO_3$ going to higher temperatures the sample coupling can not be determined anymore or is 100%. The different behavior of the sample coupling at low temperatures can be explained when looking at the different sample contributions to the total heat capacity against temperature shown in Fig. 3.4 (b). In the case of Copper at low temperatures it is dominated by the heat capacity of the addenda. Its heat capacity is so small, that other fluctuations are larger and the heat capacity is determined to be negative. The heat capacity of $SmCrO_3$ dominates the total heat capacity at low temperatures. The difference originates in the contribution of a Schottky peak to the heat capacity of $SmCrO_3$ which is discussed in a later chapter. Going to higher temperatures the percentage share of the sample heat capacity in the total heat capacity reaches a maximum. This originates in the lower Debye temperature of the samples in comparison to the sample platform. The difference in the Debye temperatures also causes the decline of the curve towards higher temperatures. Above some temperature the share of the sample heat capacity in the total heat capacity is so small, that a two τ model cannot be fit by the PPMS to the temperature rise curves anymore. Then a one τ model is used. In the one τ model the sample coupling is not determined. Thus no sample coupling or a sample coupling of 100% is determined [27]. The oscillation of the temperature rise curves is also seen in the measurement on the Copper sample with a similar mass. It is likely not a characteristic of the sample but a size effect when measuring.

As the problem of a small sample size cannot easily be fixed the measured heat capacity of Copper is compared to literature values [30, 31] and a measurement on Copper with a larger sample size that was performed by Ahmed Elghandour which

material, when being at low temperatures for longer times [27, p.13.3], is the cause of a Schottky peak at low temperatures.

are depicted in Fig. 3.5. At low temperatures the heat capacities align. Above 100 K the heat capacity of the sample with a mass of 0.74 mg starts to show fluctuations and becomes smaller than the other measurements. Too further analyze the validity of measurements with a small sample coupling due to small heat capacities the heat capacities before and after polishing the crystal are compared with measurements on a polycrystaline sample performed by Gupta and Poddar [32] in Fig. 3.6. At temperatures below 20 K the heat capacities align above they start to deviate strongly from each other.

From this it is concluded that the measurement data is feasible below 20 K. Slightly above the error may also be caused by the error introduced into the literature data

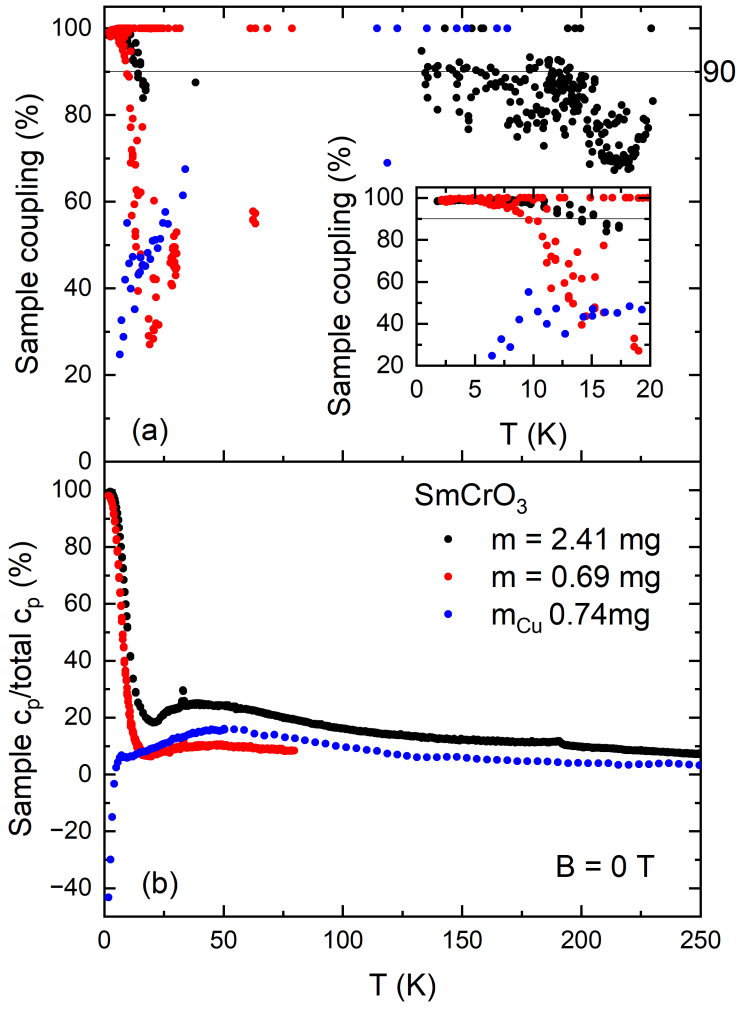


Figure 3.4: **(a)** Sample coupling versus temperature for $SmCrO_3$ with a mass of 2.41 mg and 0.69 mg and a Copper piece with a mass of 0.74 mg. **(b)** The fraction the Samples Heat Capacity makes up of the total heat capacity.

through the digitization. At temperatures above 40 K the measurements no longer give reasonable values as can be seen not only by the divergence of the measurements from the literature value but also by the divergence of the two measurements with different masses. This makes a phonon fit impossible. But the properties at low temperatures including a Schottky peak and the spin reorientation phase transition can be investigated. No field measurements were conducted before polishing, so the analysis of the effect of the field on $SmCrO_3$ is done using data obtained after polishing.

Furthermore measurements on a sample containing U^{5+} were conducted but not successful likely due to a to small sample mass of 0.33(5) mg. It was not possible to establish a sample coupling above 90% for any heat capacity measurement. Magnetisation measurements showed a sample signal in the order of micro emu which cannot be measured due to the background of the straw sample holder being of the same order of magnitude with a low reproducibility.

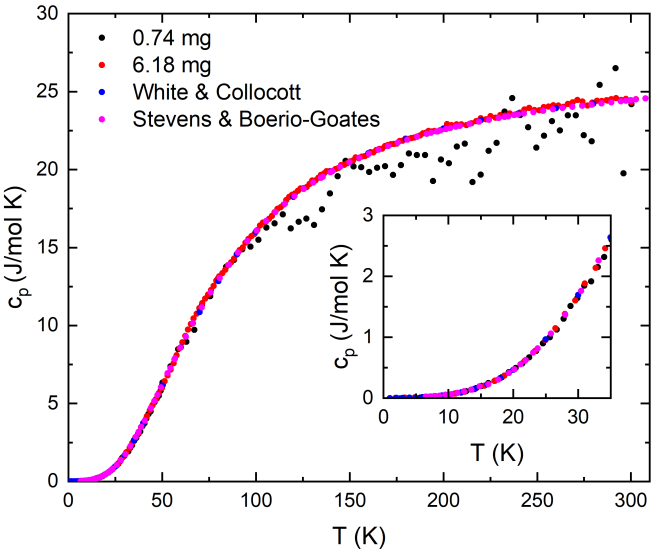


Figure 3.5: Heat capacity of Copper versus temperature for different masses and from literature ([30, 31]). Sample with mass of 6.18 mg was measured by Ahmed Elghandour using the same experimental setup.

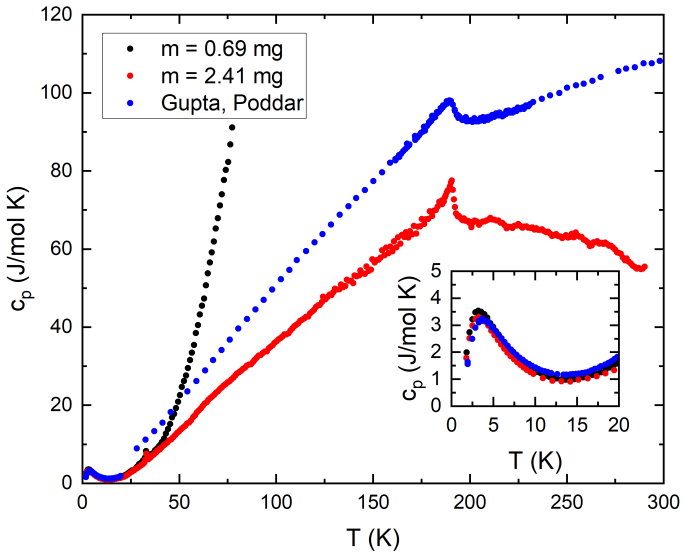


Figure 3.6: Heat capacity of $SmCrO_3$ versus temperature for different masses and from literature [32], where a polycrystalline sample was measured. The heat capacity from [32] was digitized using the Origin digitalizer for temperatures between 20 K to 50 K no precise data could be obtained.

3.2 High-Resolution Capacitance Dilatometry

In this work thermal expansion and magnetostriction measurements are performed using a mini-dilatometer from Küchler Innovative Measurement Technology [7, 33]. This instrument enables the measurement of length changes down to 1 pm [7]. The mini-dilatometer is installed in a homebuilt setup (OS), consisting of an commercial Oxford Instruments Integra AC ^{4}He cryostat [34, 21] with a variable temperature inset. This variable temperature inset provides access to temperatures between 1.5 K and 300 K. The OS also contains a superconducting magnet that can generate fields up to 15 T. Furthermore a second mini dilatometer is used in a PPMS, where temperatures down to 1.8 K and fields up to 14 T can be accessed.

This work provides only a brief introduction of the mini-dilatometer, further details are provided in [7, 35]. Figure 3.7 depicts a schematic representation of a mini-dilatometer. The principle of operation is as follows: The sample (4) is fixated in between the external frame (3) and the mobile part (1). Be-Cu flat springs (2) press the mobile part upwards. If the sample expands or contracts the springs will move the mobile part upwards or downwards respectively. The mobile part is connected to the upper capacitor plate (4) which thus also moves changing its distance to the lower capacitor plate (6) thereby changing the capacity between the two plates. The capacitance bridge AH2500A, made by Andeen-Hagerling, measures the capacitance of the capacitor in the mini-dilatometer. It is connected to the mini-dilatometer via coaxial cables and measures the capacitance with a relative precision of 5 ppm [21].

The installation of a crystal into the mini-dilatometer begins with measuring the samples thickness. Then the crystal is cleaned with an appropriate chemical and the mini-dilatometer is cleaned using ethanol. In this work Fe_3GeTe_2 is measured. It is a layered Van-der-Waals material. It was not cleaned, as the Van-der-Waals bonds may be destroyed or changed. To clean the mini-dilatometer the top part ((9)-(12) and the upper part of (3)) is removed. Subsequently, the interior is cleaned with ethanol. The crystal is then installed in the mini-dilatometer, and the top is reassembled. The distance between the capacitor plates is set such that the capacitance is 20 pF: First the screw (12) in Fig. 3.7 is unscrewed, such that it is loose. Then the cubic piston (10) is pressed down by turning the screw (9). Thereby the distance between the capacitor plates changes. When the desired capacitance is set, the screw (12) is tightened and the sample-adjusting-aid (11) is demounted.

When installing the sample in the home built setup with an Oxford cryostat (OS), the mini-dilatometer, attached to an inner sample rod, is inserted into a steel vacuum jacket. The jacket is evacuated three times with a turbo pumping station and flushed in between with helium. Following the pumping operation helium gas, as exchange gas, is inserted up to a pressure of 30 mbar. Subsequently, the jacket is sealed and inserted into the cryostat.

Before installing the sample rod in the PPMS, the sample rod is carefully heated using a heat gun, which is set to 50 °C (the mini dilatometer is not heated), to evaporate water stored on the sample rod. Subsequently, the sample rod is installed

in the PPMS, making sure that there is no leakage at the O-ring. The chamber is then alternately pumped out and flushed with helium, whereby the last cycle is a flushing cycle, which ensures that exchange gas is present in the chamber.

In this work only zero field thermal expansion measurements are shown. They are measured with the sequence:

1. Cool down to 2 K with a rate of $3\,\mathrm{K\,min^{-1}}$.
2. Beginn procedure to relax the sample and cell by heating up to 60 K with $1\,\mathrm{K\,min^{-1}}$.
3. Cool down to 2 K with a rate of $0.67\,\mathrm{K\,min^{-1}}$.
4. Cool down to 1.7 K for the OS and 1.8 K for the PPMS with a rate of $0.3\,\mathrm{K\,min^{-1}}$
5. Heat up to 305 K with a rate of $0.3\,\mathrm{K\,min^{-1}}$.

Only the data taken while heating up to 305 K is further analyzed.

Before measuring magnetostriction, the sample chamber is cooled (with the sample inside) and the sample is allowed to thermalize for 240 min. The magnetic field is then swept at a rate of 50 Oe/sec. After the upward sweep, a waiting period of between five minutes and one hour is implemented and the field is swept down again.

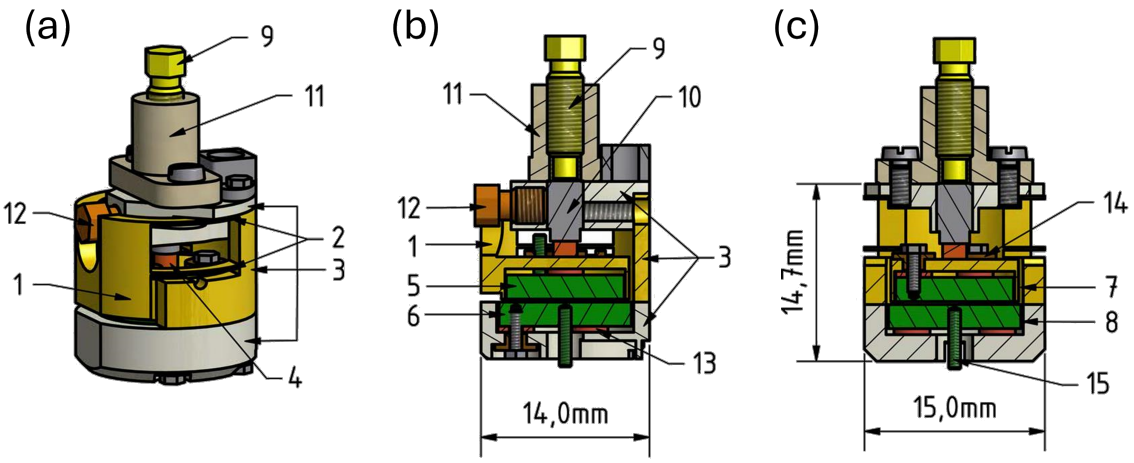


Figure 3.7: Schematic view of the mini-dilatometer **(a)** a 3D-view, **(b)** side cut-away view, **(c)** front cut-away view. (1) mobile part, (2) Be-Cu flat springs, (3) external frame, (4) sample, (5) upper capacitor plate, (6) lower capacitor plate, (7 and 8) guard rings, (9) adjusting screw, (10) cubic piston, (11) sample-adjusting-aid, (12) lock screw, (13) sapphire-washer, (14) insulating piece of Vespel, (15) electrical connection. Modified, from [7].

3.2.1 Cell Effect

The following is from [35]. When changing temperature or field the cell also expands changing the distance between the capacitor plates and thus the capacitance changes. The measured data thus includes a contribution from the cell:

$$\Delta L_{\text{meas}}^{\text{sample}} = \Delta L^{\text{sample}} - \Delta L^{\text{cell}}. \tag{3.5}$$

Where $\Delta L_{\text{meas}}^{\text{sample}}$ is the measured length change, ΔL^{sample} is the length change caused by the sample and ΔL^{cell} is the change of the cell, the cell effect. To determine the cell effect a reference measurement with high-purity copper (99.999%) with approximately the same thickness as the sample is performed. By calculating the difference between the literature length change $\Delta L_{\text{lit}}^{\text{Cu}}$ and measured length change $L_{\text{meas}}^{\text{Cu}}$ for Copper the cell effect is obtained[3]:

$$\Delta L^{\text{cell}} = \Delta L_{\text{lit}}^{\text{Cu}} - \Delta L_{\text{meas}}^{\text{Cu}}. \tag{3.6}$$

Using eq. 3.5 and eq. 3.6 the length change of the sample can be calculated:

$$\Delta L^{\text{sample}} = \Delta L_{\text{meas}}^{\text{sample}} - \Delta L_{\text{meas}}^{\text{Cu}} + \Delta L_{\text{lit}}^{\text{Cu}}. \tag{3.7}$$

From this follows, that the relative length changes of the sample can be calculated by:

$$\left(\frac{\Delta L}{L_0}\right)^{\text{sample}} = \frac{\Delta L_{\text{meas}}^{\text{sample}} - \Delta L_{\text{meas}}^{\text{Cu}}}{L_0} + \left(\frac{\Delta L}{L}\right)_{\text{lit}}^{\text{Cu}} \tag{3.8}$$

where L_0 is the length of the sample before the measurement. A correction of the cell effect is only performed for thermal expansion measurements and not the magnetostriction measurements. The cell effect is of the order of $2 - 3 \cdot 10^{-7}$ for magnetistriction measurements [34], which is 2 orders of magnitudes smaller than the relative length changes of the sample measured in this work.

The Fe_3GeTe_2 measured in this work has a thickness of 0.268 mm along the c axis. This is a rather small sample size to perform dilatometric measurements on, for comparison the materials measured in [35] have a size of 4 mm along the measured axis. As not all crystals can be grown to any size along all axes the effect of the thickness on the measurement is investigated.

To investigate the influence of thickness on the measurement, measurements on aluminium pieces with a size of 0.380 mm and 1.92 mm are conducted. The cell effect is determined using a piece of copper of similar thickness to the aluminium piece. Figure 3.8 shows the relative length changes $^{dL}/_{L}$ of the aluminium pieces and literature in dependency of temperature [36]. The measurements were conducted in

[3] When determining the cell effect with a copper measurement the cell effect does not only contain expansion of the cell but also other sources that influence the measurement. Note that it does not contain errors that are dependant on the thermal expansion of the sample for example an error that depends on the distance of the capacitor plates. This could be improved, by performing the measurement from which the cell effect is determined with a sample that has a similar thermal expansion as the sample for which the thermal expansion is to be determined.

the PPMS (a) and the OS (b). All datasets show a similar form, a convex thermal expansion at low temperature followed by a parabula like thermal expansion. In Fig. 3.8 (a) the 1.92 mm dataset is smaller than the literature dataset, the difference increases with increasing temperature. The two datasets measured with the 0.38 mm piece are different, although measured with the same procedure, indicating an uncertainty of the order of 24% at 200 K. The dataset measured second denoted as 0.380 mm 2 has larger relative length changes than the literature dataset. The dataset obtained first denoted as 0.380 mm has larger relative length changes below approximately 120 K and smaller relative length changes for higher temperatures than the literature dataset. A dataset that is smaller than the literature dataset is obtained by measuring the aluminum piece with a thickness of 1.920 mm. Although it is smaller than the dataset from literature it shows the smallest deviation to the literature dataset of the measured results. The dataset obtained by measuring the aluminium piece with a thickness of 0.380 mm is smaller than literature and deviates more from it than the dataset obtained with the aluminium piece with a thickness of 1.920 mm in the OS.

Fig. 3.9 shows the thermal expansion coefficients α of the datasets shown in Fig. 3.8. Fig. 3.8 (a) depicts the measurements performed in the PPMS with no applied field. The dataset from literature shows a shape that is similar to the shape of heat capacity in the Debye model [36]. The curve measured with an aluminium piece with a thickness of 1.920 mm behaves similar to the dataset from literature but seems to be compressed by a factor. Furthermore, it shows an anomaly from 210 K to 238 K. The origin of this anomaly is not clear, it has been consistently measured with different samples in the PPMS. Thus different causes have been suggested, with one being that there is oxide on the surface of the cubic piston in the mini-dilatometer ((10) in Fig. 3.7 (b)), but the mini-dilatometer installed in the OS does not show

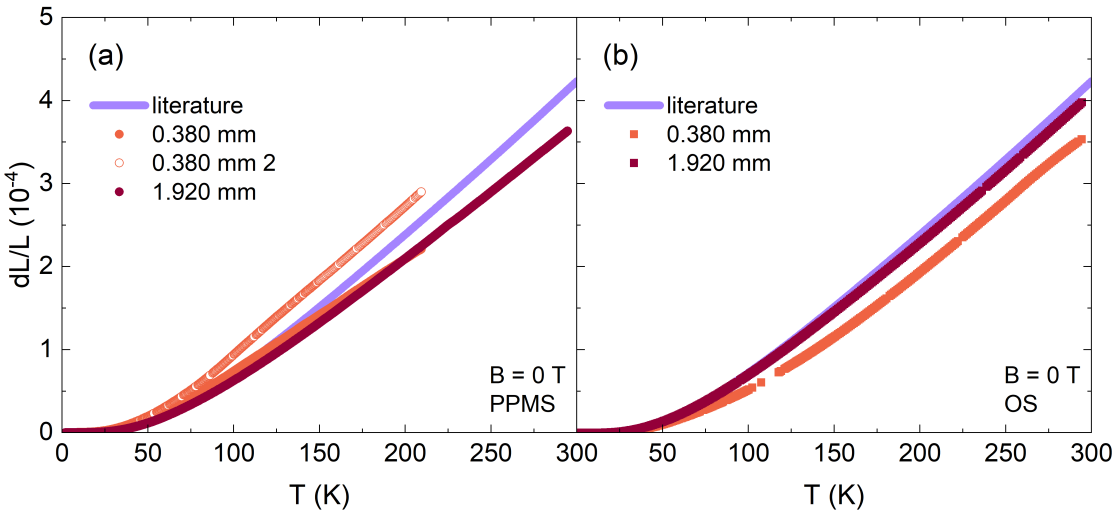


Figure 3.8: Relative length changes of aluminium against temperature measured in **(a)** PPMS and **(b)** OS no external field was applied. Measurements were performed with two aluminium pieces with different length as denoted in the legend. Literature dataset from [36].

this behaviour. An observation made by Küchler is that he has seen this in some but not all data measured in different PPMS [37]. From this observation it is followed, that water or another contamination in the sample chamber is a likely cause. The two measurements performed on the aluminium piece with a thickness of 0.380 mm are over and under the dataset from literature. Their shape is dominated by wiggles and broad peaks. The measurements goes up to 210 K as for larger temperatures the anomaly seen in the 1.920 mm measurement would be seen and the aim of this investigation was not to investigate the anomaly. The inset shows a zoom in below temperatures of 60 K where the measurements with the sample with a thickness of 0.380 mm already show a substantial deviation from literature. The measurement with the sample with a thickness of 1.920 mm lies below the literature but the deviation is smaller than 10%. Fig. 3.9 (b) shows the measurements on aluminium conducted in the OS. The measurement with an aluminium piece with a thickness of 1.920 mm shows the same form as the literature curve and the smallest deviation of all curves, similar to the corresponding relative length changes. Below 60 K the measurement shows no directional deviation from the literature. The measurement with an aluminium piece with a thickness of 0.380 mm lies below the literature dataset for all temperatures and shows a approximately linear region between 50 K and 200 K which is not expected from literature.

The measurements with the aluminium pieces show that in the PPMS even with samples that have the same thermal expansion as the thicker piece ($^{dL}/_{L}(200\,\mathrm{K}) \approx 4 \times 10^{-7}\,\mathrm{m}$ and $\alpha(200\,\mathrm{K}) \approx 3 \times 10^{-8}\,\mathrm{m\,K^{-1}}$) the determination of global properties (such as phonon fits) must be performed carefully as the dataset is compressed by a scalar factor in comparison to literature. In the OS the deviation is below 5% for all temperatures measured. Thus global properties can be investigated.

Measuring samples that have a thermal expansion of the order of $^{dL}/_{L}(200\,\mathrm{K}) \approx 10^{-7}\,\mathrm{m}$ and a thermal expansion coefficient of the order of $\alpha(200\,\mathrm{K}) \approx 7 \times 10^{-9}\,\mathrm{m\,K^{-1}}$) leads to broad bumps in α which makes the determination of global properties impossible. Furthermore measurements with small sample thickness are not reproducible indicating a large uncertainty. The measurement conducted with the 0.380 mm thick piece of aluminium also shows large deviations from the literature value and broad anomalies making the determination of global properties impossible. It can thus be concluded that for samples with relative length changes at $200\,\mathrm{K} \approx 10^{-7}\,\mathrm{m}$ and $\alpha(200\,\mathrm{K}) \approx 7 \times 10^{-9}\,\mathrm{m\,K^{-1}}$ the mini-dilatometer can only be used to determine features which occur in small temperature intervals as the deviation does not show these. For thin samples with sufficiently strong magnetoelastic coupling, the magnetic properties can be analysed also over broader temperature ranges. However it can still not be possible to analyze the phononic properties. The lower resolution and the limited trustworthiness of the data seen here can be mainly attributed to the absolute length change becoming smaller with decreasing sample size.

Furthermore these measurements show that the OS currently has a higher precision than the PPMS setup. To improve the PPMS setup the sample chamber is warmed

up and serviced. Furthermore the PPMS setup is improved for dilatometric measurements as specified in [33]: the capacitance bridge will be galvanically isolated from the grid using an isolating Transformer and the measurement computer will be isolated from the setup using an optical USB repeater.

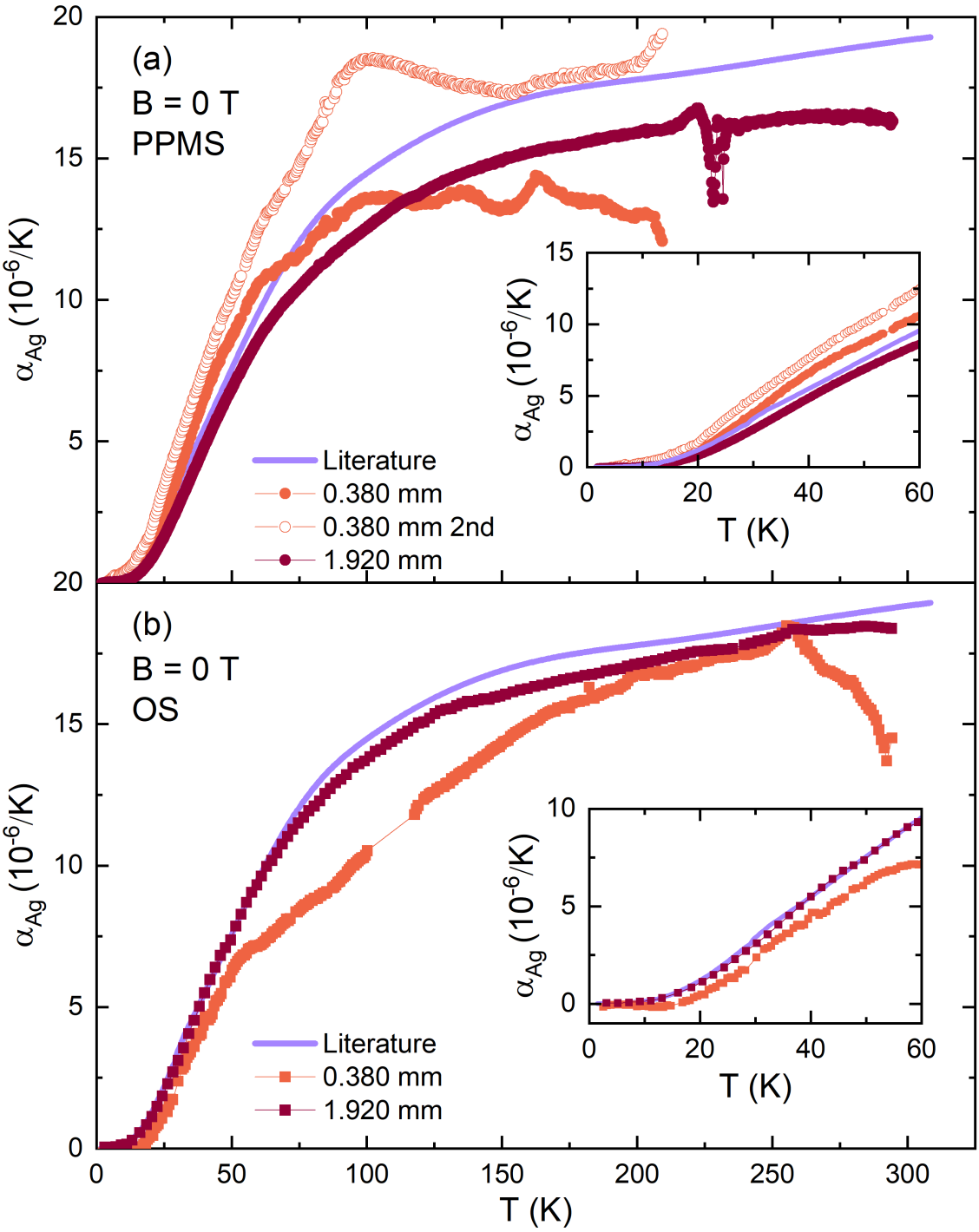


Figure 3.9: Thermal expansion coefficient of aluminium against temperature measured in the **(a)** PPMS and the **(b)** OS no external field was applied. Measurements were performed with two aluminium pieces with different length as denoted in the legend. The inset shows a zoom in of temperatures up to 60 K. Literature dataset from [36].

3.3 Magnetisation Measurements

Magnetisation measurements have been conducted using a Magnetic Properties Measurement System (MPMS3) from Quantum Design and a PPMS from Quantum Design. In the MPMS3 the DC mode was used while in the PPMS the VSM option was used.

This work only provides a brief introduction of the DC and VSM option, further details are provided in [38]. The principle working method of the DC option is that the sample holder is passed through a coil which picks up the resulting flux produced by the sample being moved through it. At different positions of the sample holder in the coil the flux through the coil is measured by a SQUID in the MPMS. In the PPMS the Voltage induced by the flux through the pick up coil is measured. While passing the sample holder through the pick up coil the environment (magnetic field, temperature) is stable. Passing the sample holder through once gives one scan. The movement of the sample holder through the pick up coil is centered around the sample position, the sample offset. From one scan the magnetisation of the sample is then extracted by fitting a dipole like model onto the measured data. The VSM option vibrates the sample holder through the pick up coil. The vibration is centered around the position where the sample is in the pick up coil. Vibrating the sample through the pick up coil leads to a change of flux through the pick up coil from which the magnetisation is determined. Acquiring data by this method is fast and thus measurements can be performed without stabilizing the environment.

The low measurement time of the VSM mode makes it possible to acquire many measurement points and perform temperature and magnetization sweeps fast in comparison to the DC mode. An advantage of the DC mode is that backgrounds subtraction is more precise as a difference in sample offset between the measurement with and without sample can be corrected after the measurement. This is not possible with the VSM mode. A difference of the sample offset can have a influence even when they are only shifted by less than a millimeter to each other.

Before measuring samples were cleaned and weighted. They were then mounted onto a quartz or a brass sample holder shown in Fig. 3.10 (a) and (b) respectively. The sample holders used in the MPMS and the PPMS are only different concerning their length. Fig. 3.10 (a) shows the Quartz sample holder of the PPMS with a sample mounted onto it using Apiezon® N-grease under a microscope. The sample was measured using the VSM mode. As the sample is very light the vibrations by the measurements do not cause the sample to detach. Fig. 3.10 (b) show a sample on the quartz piece of the brass sample holder. The two quartz pieces are pushed together to hold the sample in place.

When measuring the magnetisation in dependency of the temperature either the magnetic field was already applied while cooling (FC measurement) or the magnetic field was applied after cooling but before measuring (ZFC measurement). Measurements were always performed while the temperature increased.

Additionally to magnetisation measurements conducted on $SmCrO_3$ and Fe_3GeTe_2 magnetisation measurement were conducted on $RbCd_2Bi_2$ and $BaAg_{1.8}Bi_2$. The magnetisations of the $RbCd_2Bi_2$ and $BaAg_{1.8}Bi_2$ samples did not show a large enough magnetisation to be measured above 1.8 K. But the measurements on the $BaAg_{1.8}Bi_2$ sample did show a small contribution of a brillouinfunction with a spin of two in the isothermal magnetisation curve at 1.8 K. It is attributed to a niobium impurity of a few permille up to a percent in the sample which was introduced by growing the crystal in a niobium tube.

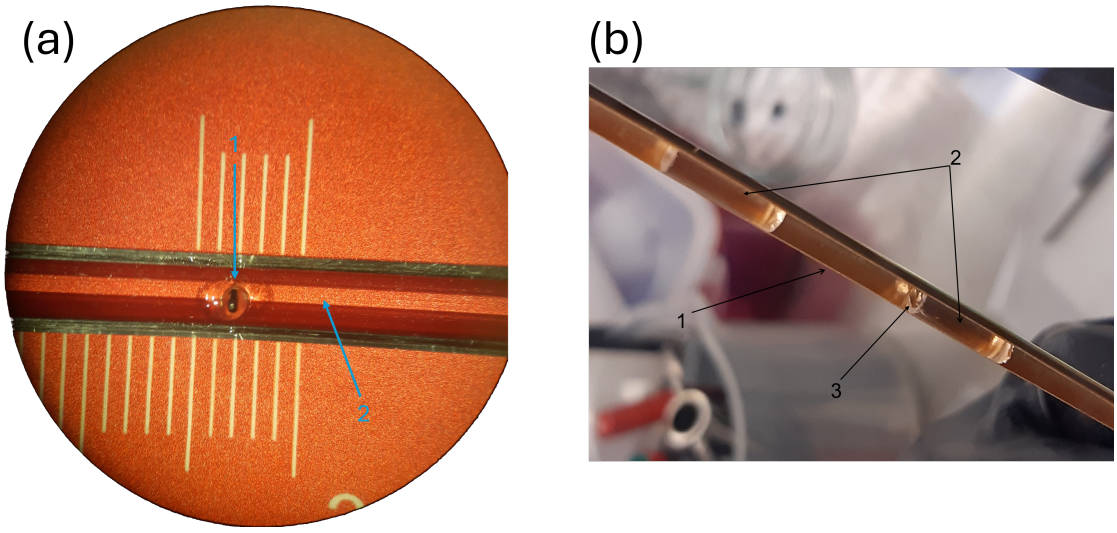


Figure 3.10: **(a)** Quartz sample holder of the PPMS on the sample mounting station photographed through a microscope. (1) Quartz sample holder (2) sample mounted with N-grease. **(b)** Brass sample holder of MPMS. In the Brasstube (1) are two quartz pieces (2), which are pushed together to hold the sample (3) in place.

Chapter 4

Dilatometric Measurements on Fe_3GeTe_2

This chapter presents thermal expansion and magnetostriction data obtained from high-resolution dilatometry measurements on Fe_3GeTe_2. To accurately understand and interpret the data it is supplemented by specific heat and magnetisation measurements.

Van-der-Waals materials are an intriguing material class exhibiting magnetic long range order down to the monolayer in the case of Fe_3GeTe_2 [3]. The long range order in Fe_3GeTe_2 at the monolayer limit is stabilized by magnetocrystalline anisotropy arising from spin orbit coupling [5]. Furthermore the transition temperature of the formation of long range order can be greatly enhanced up to room temperature for three layer samples by doping with lithium ions [5]. Combined with the stability at ambient conditions these findings render Fe_3GeTe_2 as an optimal material for further fundamental research and future applications in microelectronic devices [5].

Fe_3GeTe_2 is a layered material which crystallizes in the $P6_3/mmc$ space group. Figure 4.1 (a) depicts a top view of a Fe_3GeTe_2 layer whose structure is made up of hexagons. Their edges are occupied alternatingly by iron (labeled as Fe1) and tellurium atoms. The center of each hexagon is occupied by a germanium atom. Furthermore a unit cell is depicted. Figure 4.1 (b) shows the structure with the point of view rotated by 90° in comparison to Fig. 4.1 (a). Two layers that interact by van-der-Waals (VdW) forces are shown. A layer can be sepearated into 3 parts. The upper and the lower parts consist of the tellurium atoms and the iron atoms in the position Fe1 that make up the hexagons shown in Fig. 4.1 (a). The middle part consists of the germanium atoms and additional iron atoms (labeled Fe2) that were hidden in Fig. 4.1 (a) by tellurium atoms. A larger Fe2 occupation deficiency reduces the temperature of the ferromagnetic phase transition $T_c = 220\,\mathrm{K}$ [39, 40]. T_c is furthermore reduced by the application of uniaxial pressure [41]. Upon application of uniaxial tensile strain of 0.32% to thin flakes the coercive field increases by 150% [42] highlighting the importance of magnetoelastic coupling in Fe_3GeTe_2. To deepen the understanding of the interplay between lattice and magnetism in Fe_3GeTe_2 high

resolution capacitance dilatometry measurements are performed in this work.

Single crystals of Fe_3GeTe_2 were grown and provided by Reinhard Kremer and Eva Brücher. The crystals were grown from a stoichiometric mixture of powders of the elements Fe, Ge and Te using a minute amount of iodine as mineralizer. The growth process was conducted in evacuated quartz glass tubes in a two-zone furnace at temperatures between 650 °C and 750 °C [39]. Fig. 4.1 (c) shows the sample used in measurements performed in this thesis. It has a grayish color and exhibits a thickness of 0.268(1) mm along the c axis that is orthogonal to the image plane in Fig. 4.1 (c). Dilatometric measurements were performed along the c axis with the magnetic field applied parallel to it.

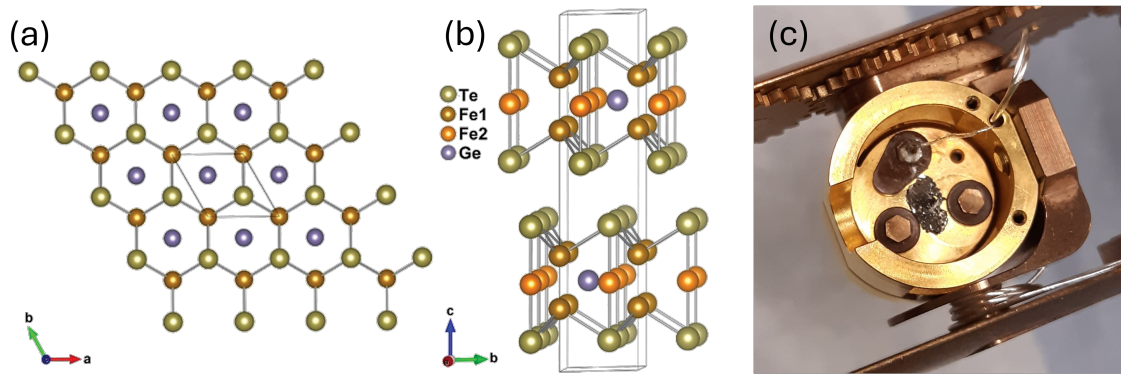


Figure 4.1: **(a)** Top view on the schematic crystal structure with unit cell and **(b)** side view with unit cell of Fe_3GeTe_2. **(c)** Fe_3GeTe_2 sample in the open dilatometer cell. The c axis is orthogonal to the plane of the image. (a) and (b) are modified from [43].

4.1 Thermal Expansion Measurements

Figure 4.2 shows the relative length changes dL_c/L_c and their temperature derivative α_c as a function of temperature in zero magnetic field. The measurements were performed in the homebuilt setup specified in chapter 3.2 (OS). The relative length changes show konvex temperature dependence at temperatures below 150 K. For larger temperatures the T dependency is rather linear. At 216 K there is a jump superimposed onto the linear part shown in the inset. The pink lines approximate the linear part. Because of the jump they do not lie on each other. The thermal expansion coefficient rises up to 160 K and stagnates above. Broad bumps at 80 K, 160 K, a wiggle above 270 K and an anomaly with a maximum at 216 K can be seen. The cause for the broad bumps and the wiggle above 270 K is the measurement accuracy. As the sample is only 0.268(1) mm thick the changes per Kelvin seen here are of the order of 1 nm. In principle it is possible to see length changes of the order of 1 pm with the dilatometer [7]. For samples such as the Fe_3GeTe_2 measured in this work the resolution limit is reached if one wants to look at the global properties of the material (see chapter 3.2.1) [37]. These broad bumps are

superimposed on the lattice expansion over large temperature intervals making a phononic fit impossible. The anomaly at 216 K in α_c is also seen in the relative length

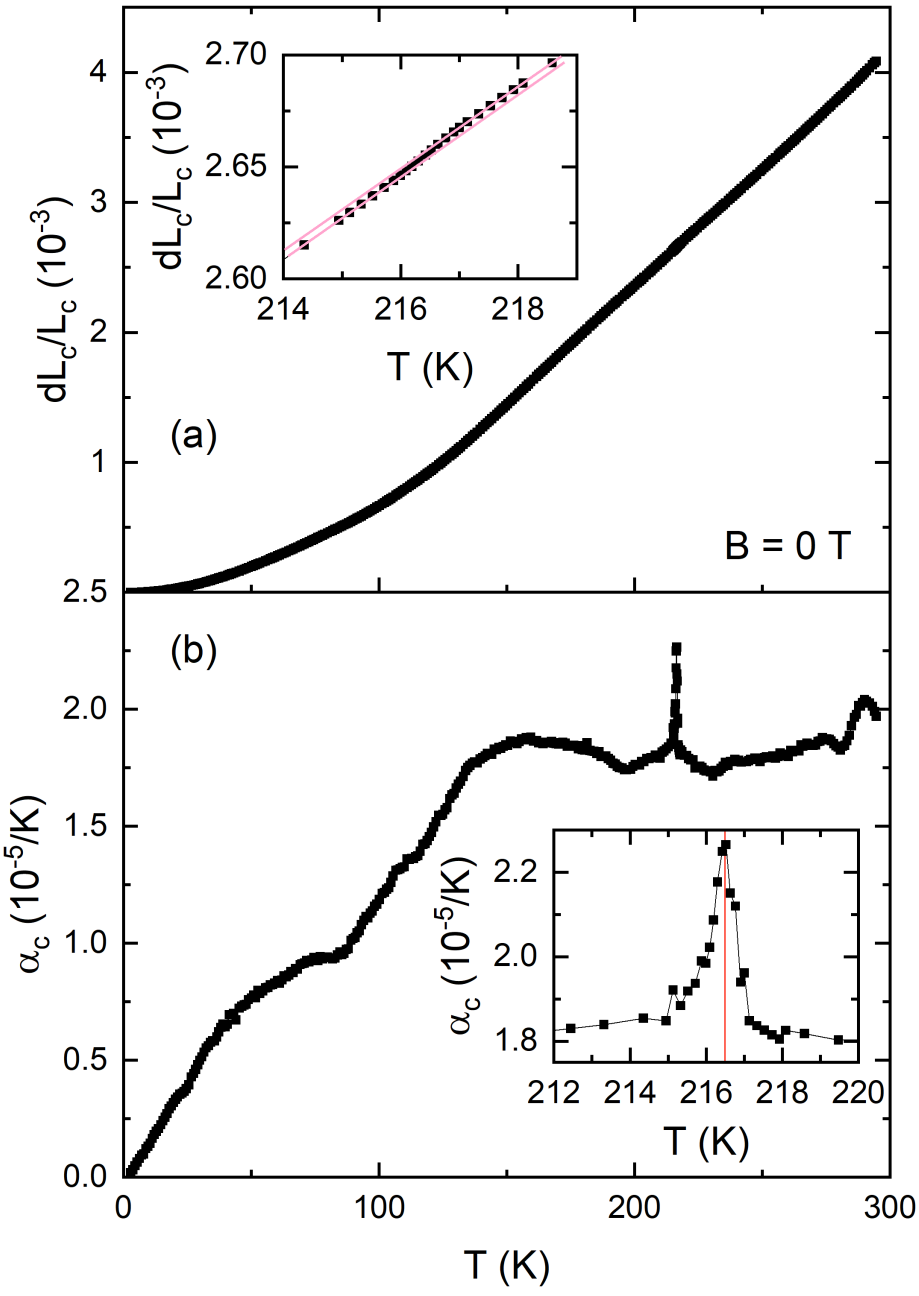


Figure 4.2: **(a)** Relative length changes of Fe_3GeTe_2 measured along the c axis without an applied field as a function of temperature. **(b)** Corresponding thermal expansion coefficient. The insets depict a zoom in of the anomaly at 216 K. The pink lines in the inset of (a) are a guide to the eye.

changes and shown in the inset. It can be attributed to the ferromagnetic phase transition [44]. A magnetoelastic coupling which causes the ferromagnetic phase transition to be visible in α_c as an anomaly is to be expected as an influence of strain on the magnetic properites of Fe_3GeTe_2 has been reported before [8]. The vertical line in the inset of 4.2 (b) goes through the maximum of the peak. The right side of the anomaly drops off faster than the rise of the left side making the anomaly non symmetric although it appears to be symmetric when looking at 4.2 (b). The peak appears to have a λ-like form which one would expect as the phase transition is a ferromagnetic phase transition. However it cannot be ruled out, that the background contributes an anomaly that causes this asymmetry. Although it is not possible to perform a Debye fit to isolate the magnetic contribution to α_c it is scaled to the heat capacity in the vicinity of the ferromagnetic phase transition. Figure 4.2 shows the thermal expansion coefficient and the heat capacity from Kremer and Brücher [39] in the temperature range from 190 K to 240 K. The axis are scaled such that the heat capacity data and thermal expansion overlap between 200 K and 215 K. But the anomalies in α and c_p are not scalable to each other. A scaling is made impossible due to the thin anomaly in α_c which the heat capacity is lacking and the different behavior above the anomaly. The different behavior above the anomaly could be caused by the measurement resolution as described before.

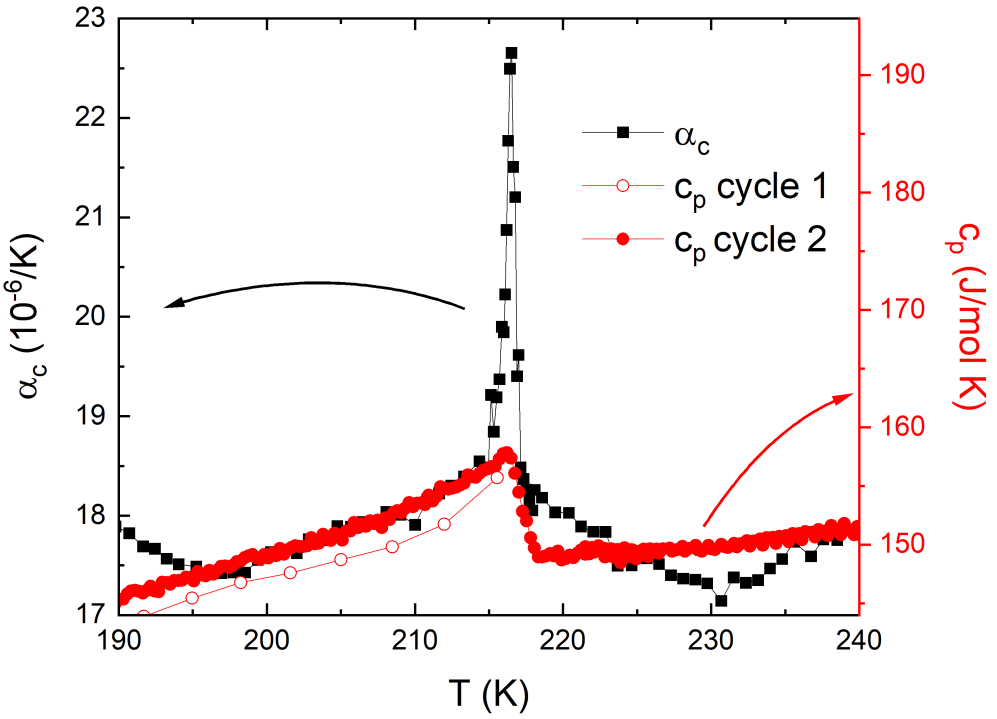


Figure 4.3: Detailed view around the anomaly of the thermal expansion coefficient and zero field heat capacity measured by Kremer and Brücher [39] as a function of temperature. Heat capacity data with open circles are from a different measurement cycle.

4.2 Magnetostriction Measurements

Fig. 4.4 depicts magnetistriction measurements along the c axis versus magnetic field parallel to the c axis in the PPMS and the OS setup. Measurements were obtained while increasing the field (up sweep) and decreasing the field (down sweep). The data was obtained at a temperature of 2 K. Starting at $B = 0$ and increasing the field the data show an expansion and a kink at approximately 0.4 T in the up and in the down sweep. For fields larger than the field that the kink occurs at the up sweeps show a concave behavior except for the up sweep labeled as 5 PPMS. The two up sweeps measured to different magnetic fields in the OS do not deviate from each other. But the two curves measured in the PPMS deviate from each other and from the curves measured in the OS as they show different curvatures. Furthermore the measurements in the OS show a contraction of the material, while the measurements in the PPMS show an expansion. The down sweeps all show a convex temperature dependence although the curvature varies largely with the 14 PPMS measurement having the larges curvature, the measurements conducted in the OS having approximately the same curvature and the 5 PPMS having the smallest curvature. The concave and convex behavior in up and down sweep lead to a hysteresis forming in each measurement cycle consisting of an up and down

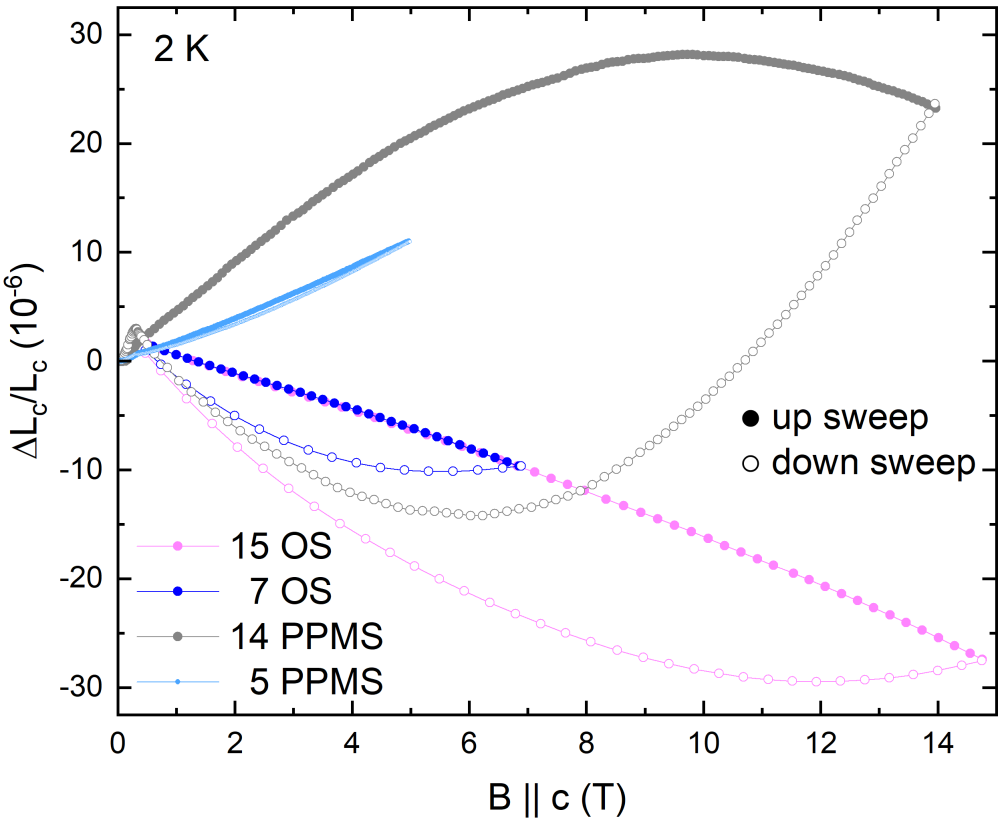


Figure 4.4: Magnetostriction measured along the c axis as a function of the magnetic field along the c axis. The legend notes the maximum field at which data points where taken for the curve and the device used to measure the data.

sweep. The measurement cycles were conducted up to different fields. Even when taking this into account the size of the hysteresis varies greatly due to the different size of the curvatures and follows no simple dependency on the magnetic field. The concave and convex form of up and down sweep lead to a butterfly like shape of a measurement cycle. Butterfly like shapes in magnetostriction appears in models containing domain wall translation [45]. But one would expect to see these domain wall effects in the magnetisation as a hysteresis which is not observed (inset Fig. 4.5). The different non compatible behavior of magnetistriction datasets measured in the OS and the PPMS further complicate the interpretation of the measured data.

Fig. 4.5 (a) shows a zoom in of the magnetostriction measured in the OS between 0 T and 1 T at 2 K. Below a magnetic field of 0.5 T Fe_3GeTe_2 expands with rising field up to a kink at 0.3 T in the down sweep and 0.4 T in the up sweep. At higher fields the afore mentioned hysteresis opens. Fig. 4.5 (b) shows the magnetisation measured with a field applied along the c axis the inset depicts all magnetisation data obtained. The magnetisation of Fe_3GeTe_2 can be divided into two regimes. A first regime at small fields where the magnetisation rises strongly followed by a second regime where the magnetisation is in saturation. The magnetisation saturates at approximately 1.50(5) μ_B/Fe which is higher than the reported values of 1.2μ_B/Fe found for $Fe_{2.83}GeTe_2$ [44] and approximately 1.3μ_B/Fe found for a sample with the same element composition of $Fe_{2.92(1)}Ge_{1.02(3)}Te_2$ as the sample investigated here [39]. The origin of the high saturation magnetisation in the sample investigated in this work is not known. The transition between the two regimes takes place at 0.45 T for the up sweep and 0.35 T for the down sweep. These applied fields approximately match with the field of the transition between the two regimes in the magnetostriction. That the magnetisation is in saturation above 0.45 T makes it extremely unlikely, that the hysteresis at higher fields is caused by a torque whose origin are the magnetic moments in the magnetic field. The magnetostriction can thus be divided into two parts. At small fields it is influenced by the moments that are aligning with the magnetic fields. At higher fields a hysteresis occurs whichs origin remains elusive.

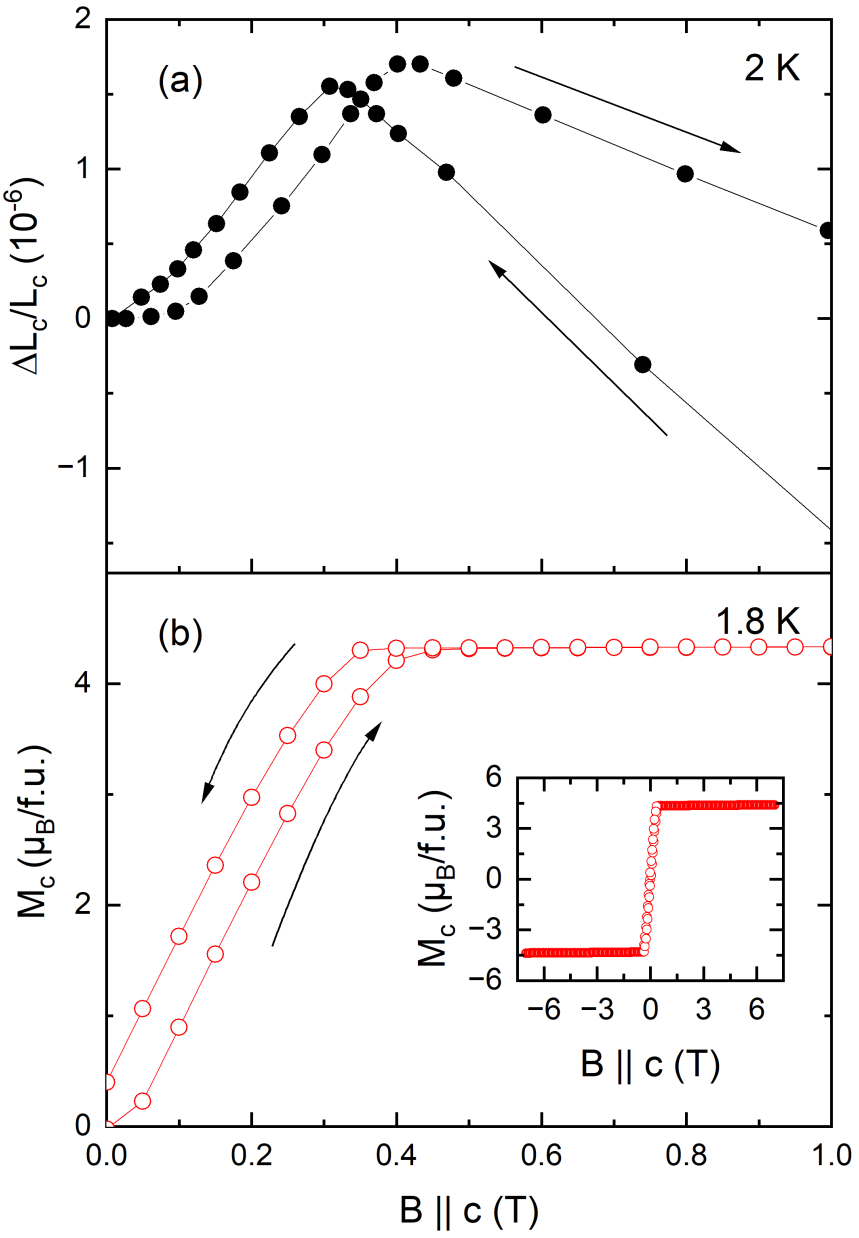


Figure 4.5: **(a)** Magnetostriction measured along c axis in the OS against the magnetic field parallel to the c axis up to 15 T. **(b)** Magnetisation measured versus magnetic field parallel to the c axis. The inset shows the whole measurement interval of the magnetisation data.

Chapter 5

$SmCrO_3$

5.1 Introduction

The structure of $SmCrO_3$ is shown in Fig. 5.1. It can be classified as a distorted perovskite structure and belongs to the space group *Pbnm* or *Pnma* from the orthorombic crystal system [1]. The Cr^{3+}-ions are centered in an octahedron formed by the O^{2-}-ions that are located at the edges of the octahedron. Neighboring octahedra share an oxygen ion. The Sm^{3+}-ions are located in between the octahedra.The magnetism in $SmCrO_3$ is caused by the 3d electrons of the Cr^{3+}-ions and the 4f elec-

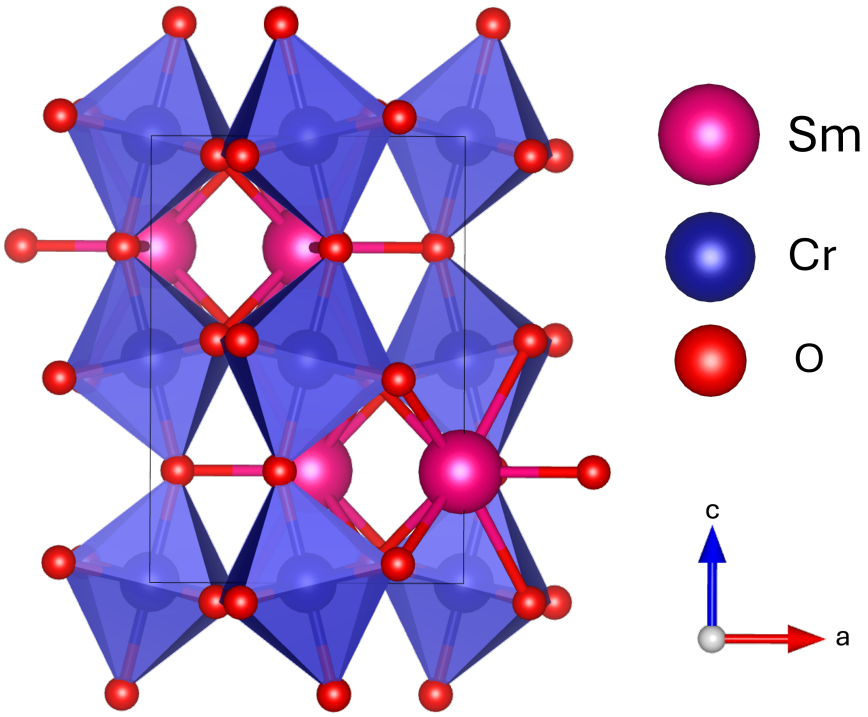


Figure 5.1: Schematic of the structure of $SmCrO_3$. Image is created with Vesta [46] using the ICSD file 251099 [47].

trons of the Sm^{3+}-ions. Fig. 5.2 (a) shows the magnetic susceptibility as a function of temperature, measured at a static magnetic field of $B = 0.01\,\mathrm{T}$ applied along all three main crystallographic axes [1]. The measurements are performed in the field cooled mode. For the magnetic field applied along the a and c axis, zero field cooled measurements are additionally shown. Two distinct features can be seen in all datasets: A sudden change in magnetisation at a temperature of 33 K and at a temperature of 192 K. These two features show that there are at least three phases in the material. At temperatures above 192 K, the susceptibility is low and independent of the direction of the applied magnetic field. The magnetic moments are not long-range ordered and the corresponding phase is the paramagnetic phase [1]. Below 192 K down to 33 K, the magnetic susceptibility increases drastically when the field is applied along the c axis. When applied along the a and b axis, a slight increase is still visible. Neutron scattering experiments show, that the magnetic moments of the chromium atoms are in the antiferromagnetic Γ_4 configuration here [48, 49, 50]. This configuration is shown in Fig. 5.3 (c). The light green arrows symbolize the direction of the magnetic moments of the chromium ions and the dark green arrows symbolize the resulting magnetic moment. In the Γ_4 configuration, the chromium moments are in the ab plane. Neighboring moments are not perfectly anti parallel. Instead, they are tilted to each other resulting in a ferromagnetic moment along the c axis [51, 9, 10]. These weak ferromagnetic moments cause the highly anisotropic behaviour of the susceptibility between 33 K and 192 K.

If the temperature drops below 33 K, a decrease of the susceptibility with magnetic field applied along the c direction and an increase in the susceptibility with magnetic field applied along the a or b direction occurs. This indicates a spin reorientation transition (SRT) at which the moments rotate such that the weak ferromagnetic moments are in the ab plane below 33 K [1, 48, 49, 50]. There are two possible configurations for the magnetic moments of the chromium ions: The Γ_2 configuration, in which the moments have a non zero component along the c axis and a resulting magnetic moment in the ab plane, and the Γ_1 configuration, where the chromium moments lie in the ab plane and there is no resulting magnetic moment [51, 9, 10].

The exact configuration of the magnetic moments of the chromium ions remains unclear and is closely connected to whether the SRT is a continous or discontinous phase transition. Neutron scattering experiments with high energy (hot) neutrons reveal the coexistence of the Γ_1 phase and the Γ_4 phase near the phase transition. Furthermore it was concluded, that the SRT is a discontinuous phase transition [12]. In contradiction to this conclusion, Sau et al. [13] noted that the use of hot neutrons leads to a low resolution of the scattering data and a mixing of the magnetic peaks with the nuclear peaks [13]. Instead, their measurements show that the SRT corresponds to a change in the spin configuration from Γ_4 to Γ_2, suggesting a continous phase transition [13]. Furthermore DFT calculations show that the Γ_2 configuration is lower in energy than the Γ_1 configuration [13]. The magnetization as a function of temperature at constant magnetic field was measured by Sau et al. A hysteresis was obtained when first decreasing and then increasing the temperature in the vicinity of the SRT [14]. It was concluded, that the phase transition is made

up of a continuous rotation followed by a discontinuous transition into a different spin configuration [14]. Magnetization measurements on a $SmCrO_3$ single crystal conducted by Yuan et al. show a spin configuration that is not strictly a Γ_1 or a Γ_2 configuration but a mixed or inhomogeneous spin configuration [1]. Furthermore these measurements do not show a hysteresis in the vicinity of the SRT, indicating a continuous transition [1].

Below a temperature of 16 K the fc and zfc curves split, as seen in Fig. 5.2 (a). The splitting of fc and zfc curve is larger when measuring along the a axis than

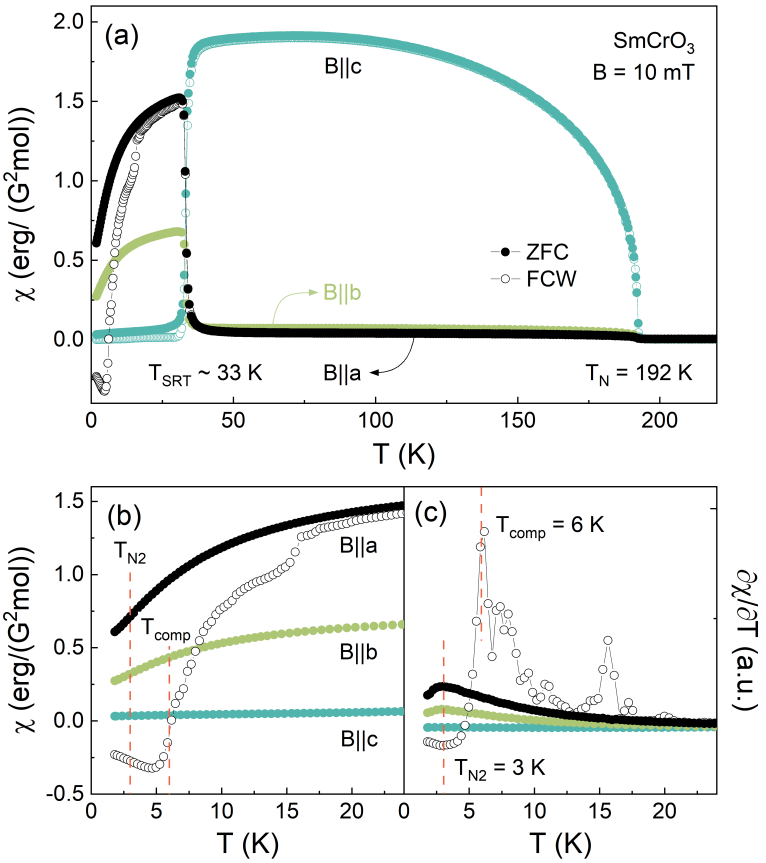


Figure 5.2: Magnetic susceptibility χ at B = 0.01 T against temperature. **(a)** Temperature dependence of $\chi = M/B$ for magnetic fields along the crystallographic a, b and c direction. Data with full points is field cooled, data with open points zero field cooled. **(b)** Magnetic susceptibility at lower temperatures. T_N, T_{N2} and T_{SRT} T_{N2} are highlighted. **(c)** The derivative of the Magnetic susceptibility with respect to the temperature. Image from [1].

when measuring along the c axis. The splitting confirms the presence of a weak ferromagnetic moment [1]. A zoom in of the fc and zfc curves in this temperature region is shown in Fig. 5.2 (b). With decreasing temperature, the susceptibility measured in the zfc mode vanishes at the compensation temperature marked as $T_{\mathrm{comp}} = 6\,\mathrm{K}$. At T_{comp} the samarium sublattices magnetic moment is equal to the magnetic moment of the chromium sublattice but the moments are anti parallel, thus compensating each other. Figure 5.2 (c) shows the derivative with respect to the temperature of the susceptibilities shown in Fig. 5.2 (b). At 3 K a maximum can be seen in the derivatives marked as T_{N2}. The presence of the maximum at T_{N2} and the decrease of the zfc curve of the susceptibility measured with a field applied parallel to the a axis implicate that the magnetic moments of the samarium sub lattice are ordering [1]. For larger temperatures below 192 K, the samarium moments are not ordered, but the chromium moments influence them. This causes the samarium sublattice to show weak ferromagnetic moments with a parallel alignment to the magnetic moment of the chromium sublattice [9].

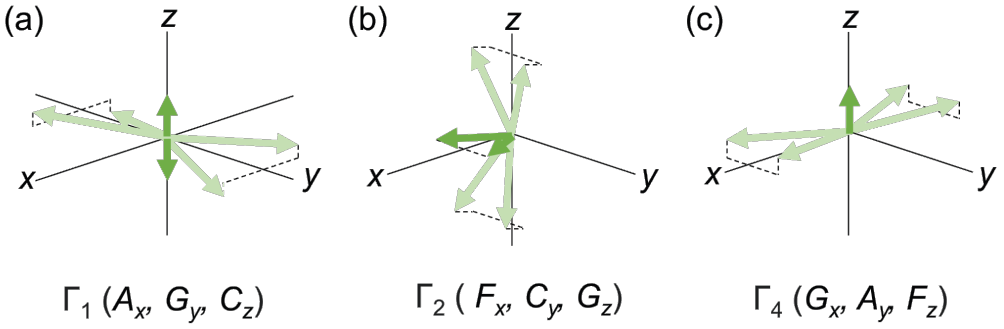


Figure 5.3: Abstractions of possible configurations for the magnetic moments of the chromium in $SmCrO_3$ [51, 9, 10]. The light and dark green arrows show the chromium magnetic moments and the resulting magnetic moments, respectively. The x, y and z axis are parallel to the crystallographic a, b and c directions, respectively. From [1], after [51].

5.1.1 Entropy Changes at T_{SRT}

To investigate the nature of the SRT the Clausius Clapeyron equation (eq. 2.5) can be used [22]. To determine the different quantities the method used in [1] was adopted. The determination of ΔM_c from the experimental data is shown in Fig. 5.4 (a) for an isothermal magnetisation curve at 15 K. In the figure the magnetisation versus the applied magnetic field in the direction of the c axis and the derivative of the magnetization with respect to the applied magnetic field are shown. At high and low fields the magnetisation increases linearly with the magnetic field. The magnetic fields at which the magnetisation increases linearly are separated by a broad jump centered at 9.09(10) T. The jump in magnetization is identified as ΔM_c. The magnetic field B_c at which it occurs is determined from the maximum of the derivative of the magnetisation as shown in Fig. 5.4 (a) and varies with temperature. To determine ΔM_c linear fits are performed to the linear parts in the magnetization below and above ΔM_c. Then the difference between the linear fits is calculated at B_c. The isothermal magnetisation measurement data at other temperatures is shown in 5.5 (a). The jump in magnetisation in isothermal magnetisation datasets above 20 K and one of the two datapoints from isothermal magnetisation curves at 20 K were determined in [1]. Figure 5.4 (b) shows B_c as deduced by the above mentioned procedure for different temperature from the data shown in Fig. 5.5 (b) To determine $^{\partial B_c}/_{\partial T}$, two linear fits to B_c for $T \geq 13.5\,\mathrm{K}$ (yellow line in Fig. 5.4 (b)) and $T \leq 15\,\mathrm{K}$ (blue line in Fig. 5.4 (b)) were performed. To determine the entropy change in the SRT ΔS_{SRT}, the Clausius-Clapeyron equation (eq. 2.5) is used. Therefore the parameters of $-0.50(3)\,\mathrm{T\,K^{-1}}$ (for $T \geq 13.5\,\mathrm{K}$) and $-0.70(3)\,\mathrm{T\,K^{-1}}$ (for $T \leq 15\,\mathrm{K}$) are inserted for $^{\partial B_c}/_{\partial T}$ together with the values determined for ΔM_c.

Fig. 5.4 (c) shows the resulting entropy change in the SRT for magnetic fields applied along the a and c axis respectively. The values for magnetic field applied along the a axis are from [1], the data points for the applied field along the c axis for magnetic fields smaller than $B_c = 6.3\,\mathrm{T}$ determined in this work are from measurements reported in [1].

For the magnetic field applied along the c axis, the entropy change rises linearly with increasing magnetic field up to $B_c = 5\,\mathrm{T}$. For higher B_c the slope is larger with a jump or kink from 9 to 10 T. The jump or kink could be caused by the approximation of the slope shown in Fig. 5.4 (b) by two linear fits. A determination of $^{\partial B_c}/_{\partial T}$ by a discrete derivative or a Polynomial of second order was not favorable, as the derivative lead to scattering of the entropy change values due to the measurement uncertainty and the polynomial of second order is ill fitting at temperatures above 25 K as the B_c show a linear dependency in temperature. The entropy change in the SRT determined for fields along the a axis is smaller than that determined along the c axis and is linearly dependent on the magnetic field that the SRT occurs at for $B_c \leq 3.6\,\mathrm{T}$.

For $B \leq 5\,\mathrm{T}$ and $B \leq 3.6\,\mathrm{T}$ for the magnetic field respectively applied along the c and a axis a linear approximation of $\Delta S_{SRT}(B)$ seems reasonable. A fit to the data yield $\Delta S_{SRT}(B \parallel c = 0) = 32(14)\,\mathrm{mJ\,mol^{-1}\,K^{-1}}$ and $\Delta S_{SRT}(B \parallel a = 0) =$

$-1.5(14)\,\mathrm{mJ\,mol^{-1}\,K^{-1}}$. The entropy change determined with field applied along the a axis is within the 1.1 σ-interval from $0\,\mathrm{J\,mol^{-1}\,K^{-1}}$ suggesting that the negative entropy change is a statistical artifact.

$\Delta S_{\mathrm{SRT}}(B = 0)$ has no external magnetic field applied. Consequently, the material is subjected to the same environmental conditions in both extrapolations. Through this one can assume, that the material is in the same state for both extrapolations[1]. The deviation of the entropies determined by both extrapolations is within the 2.4σ-interval, which is no significant deviation. To determine if the entropies determined with the Clausius-Clapeyron equation are correct, the entropy change in the SRT must be determined using another method.

[1] This is a assumption, as [1] found hysteretic behaviour in isothermal magnetisation curves. At 35 K near $T_{\mathrm{SRT}} = 33.1(4)\,\mathrm{K}$ there is no remanent magnetisation in the isothermal magnetisation measurement with field along the c axis. The remanent magnetisation in the measurement with field along the a axis is of the order of $0.004\,\mu_{\mathrm{B}}$/f.u.. Calculating an entropy change with the Clausius-Clapeyron equation with this remanent magnetisation gives an entropy change of $5.4\,\mathrm{mJ\,mol^{-1}\,K^{-1}}$ amounting to roughly 10% of the difference. Note that the different remnant magnetisation indicate different internal fields not taken into account here.

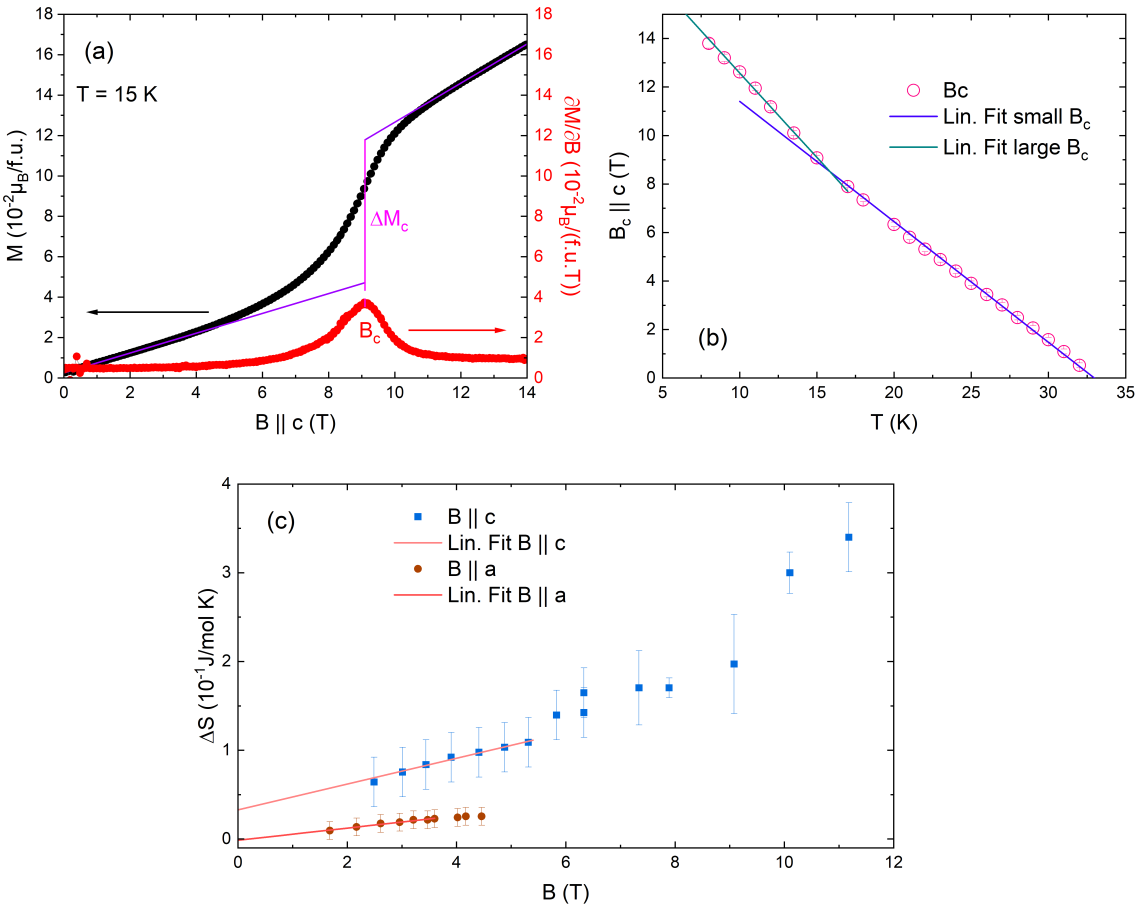


Figure 5.4: **(a)** Magnetisation and derivative of the magnetisation with respect to the magnetic field against applied magnetic field in crystallographic c direction at T = 15 K. The determination of the jump size in magnetisation at the SRT, ΔM_c, is indicated by blue lines and is described in the text. **(b)** B_c for fields parallel to the c axis as a function of temperature. The linear fits indicate the determination of $\partial B_c/\partial T$ as described in the text. **(c)** Entropy change associated with the SRT against the magnetic field at which the SRT occurs. The entropy change in the SRT is determined with the Clausius-Clapeyron equation for fields applied in crystallographic c and a direction. Solid orange and green lines illustrate linear fits performed for fields below 5.3 T for $B \parallel$ c and 3.6 T for $B \parallel$ a. The data with field applied in the crystallographic a direction are from [1], the data points below 6.3 T with field in the crystallographic c direction are determined from measurements reported in [1].

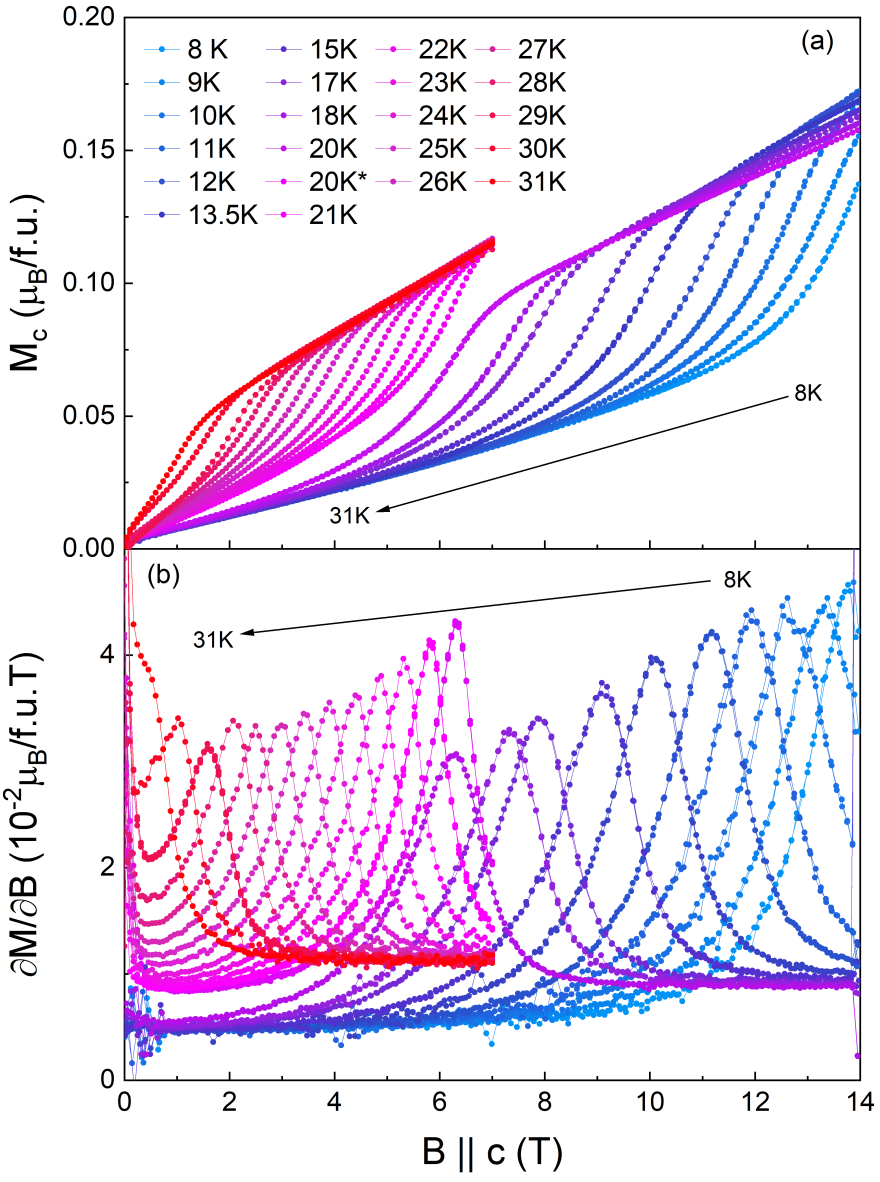


Figure 5.5: **(a)** Isothermal magnetisation and **(b)** field derivative of the magnetisation against applied magnetic field in crystallographic c direction. Isothermal magnetisation measurements measured at temperatures larger than 20 K and the one marked by* are reported in [1].

5.2 Heat Capacity Measurements

5.2.1 Heat Capacity at B = 0 T

A method to determine the entropy changes are heat capacity measurements as the heat capacity c_p is connected to the entropy S by eq. 2.11. Figure 5.6 (a) shows the zero field heat capacity measurements against temperature in the temperature range from 1.8 K to 40 K. The measurements were performed on a sample with a mass of m = 2.41(3) mg. A broad anomaly is observed at 3 K, the broadness of the anomaly suggests a Schottky peak, which will be further investigated in chapter 5.2.2. A second sharper anomaly is observed at 33 K, corresponding to the SRT a zoom in of it is depicted in the inset. Its shape appears to be symmetric and not λ like, which indicates a first order phase transition. Figure 5.6 (b) shows the heat capacity from the same measurement as the heat capacity shown in Fig. 5.6 (a) in the temperature range from 170 K to 210 K. An anomaly is observed at 190 K which is caused by the antiferromagnetic ordering of the Cr^{3+} moments [1].

The anomaly associated with the antiferromagnetic phase transition is shown in Fig. 5.7. The figure depicts the heat capacity measured in [32] in (a) and the heat capacity measured in this work in (b) from 150 K to 240 K at zero applied magnetic field. To determine the jump in heat capacity linear fits are performed above and sufficiently below the anomaly [52]. The linear fits are performed in the temperature regions where the anomaly is approximately linear as the result will be compared with mean field theory where fluctations are neglected. The dark blue lines are the best fit whereas the light blue dashed lines are a fit that is still reasonable. The pink vertical line signals the temperature of the phase transition. At its temperature the difference between the two dark blue and two light blue lines is taken to determine Δc_p. Its position can be determined from a construction of equal areas between the vertical line, the linear fits and the measurement data. But as the uncertainties are dominated by the uncertainty of the fit a precise determination of the temperature is not performed. The jump in specific heat at the phase transition is thus determined to 8.5(15) $\mathrm{J\,mol^{-1}\,K^{-1}}$ for the heat capacity measured by Gupta and Poddar [32] and to 5.6(25) $\mathrm{J\,mol^{-1}\,K^{-1}}$ from heat capacity measurements in this thesis. The values do not deviate significantly. The jump Δc_p in heat capacity at the phase transition can be calculated in a mean field approximation by [53]:

$$\Delta c_p^{\mathrm{MF}} = \frac{5Nk_{\mathrm{B}}}{2} \cdot \frac{(2S+1)^2 - 1}{(2S+1)^2 + 1}. \tag{5.1}$$

With $S = 3/2$ for $SmCrO_3$ the jump in heat capacity is calculated to $\Delta c_p^{\mathrm{MF}} \approx 18.3\,\mathrm{J\,mol^{-1}\,K^{-1}}$. The deviation between the jump in heat capacity calculated from experiment and from mean field theory is significant. The origin of this deviation might be short range order above T_N or incomplete or imperfect long-range order below T_N.

Using the Ehrenfest relation [17]:

$$\frac{dT_N}{dB} = -T_N \frac{\Delta \frac{\partial M}{\partial T}}{\Delta c_p} \tag{5.2}$$

the field dependence of the phase transition can be determined from the jump in heat capacity and the jump in the derivative of the magnetisation. T_N is the temperature of the phase transition and M is the magnetisation. Figure 5.8 shows the derivative of the susceptiblity as a function of temperature at a magnetic field of B

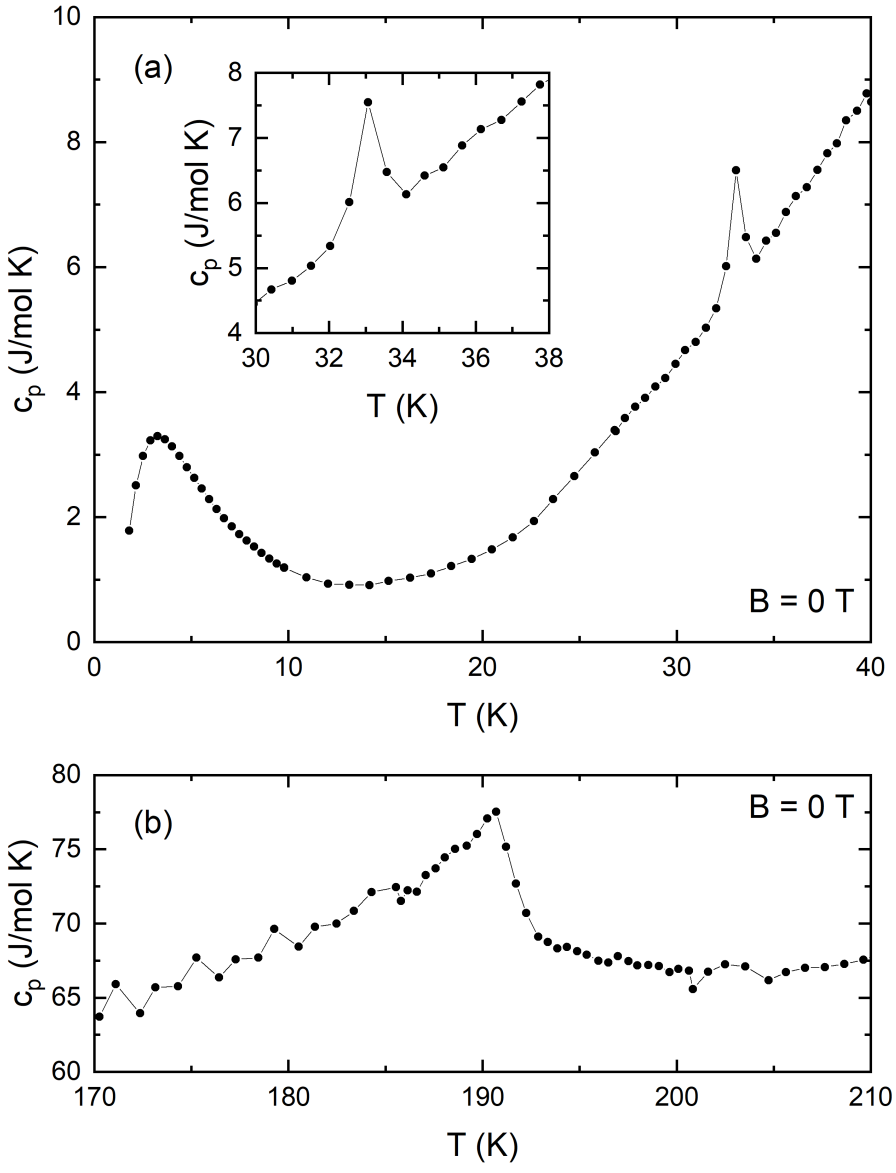


Figure 5.6: **(a)** Heat capacity as a function of temperature measured at zero magnetic field in the temperature range from 1.8 K to 40 K. The inset depicts an anomaly at 33 K. **(b)** Heat capacity from the same measurement as the heat capacity in (a) as a function of temperature measured at zero magnetic field in the temperature range from 170 K to 210 K. The measurement was performed on a crystal with m = 2.41(3) mg.

= 0.01 T applied in the crystallographic (a) c and (b) a direction. The construction is similar to that used to determine the jump in heat capacity. The dark blue lines are the best fit. Their difference is calculated at the vertical pink line marking the temperature of the phase transition. The dashed light blue lines are a fit that is also plausible and are used for the determination of the uncertainty. The jump in $\partial\chi/\partial T$ is thus determined to 0.05(3) erg G^{-2} mol^{-1} K^{-1} for an applied magnetic field along the c axis and 0.85(15) erg G^{-2} mol^{-1} K^{-1} for an applied magnetic field along the a axis. Using equation 5.2 and the obtained values[2] the temperature dependence is determined to 0.17(13) K T^{-1} for magnetic fields parallel to the c axis and 0.0029(6) K T^{-1} for magnetic field parallel to the a axis with a strength between 0 T and 0.01 T. Figure 5.9 shows the temperature at which the antiferromagnetic phase transition occurs as a function of the applied magnetic field in (a) crystallographic c direction and (b) crystallographic a direction. The darkblue line is a linear fit used to determine $\partial T/\partial B$ and the lightblue dashed line is used to determine the upper value which still seems plausible. To determine the change of temperature of the antiferromagnetic phase transition with field $\partial T/\partial B$ is determined to 0.29(6) K T^{-1} for $B \parallel c$ and 0.17(14) K T^{-1} for $B \parallel a$. The values calculated using the Ehrenfest relation and those determined from Fig. 5.9 agree within their uncertainties.

The measured heat capacity is assumed to include magnetic and phononic contributions. To determine the magnetic entropy change at the SRT it is first necessary to separate the magnetic contribution to the heat capacity from the total heat capacity which is dominated by the heat capacity of the lattice. This is achieved by subtracting a linear background in the vicinity of the SRT peak, which serves as an

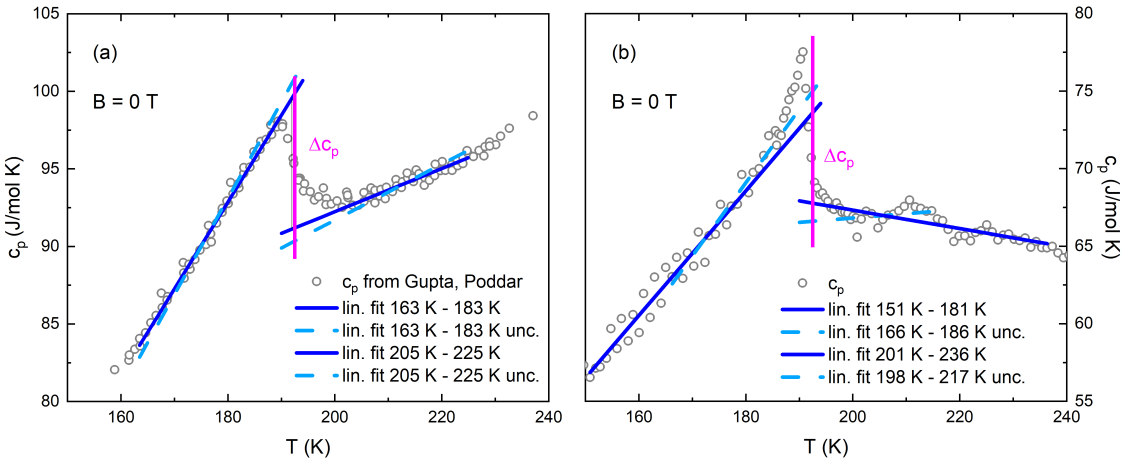


Figure 5.7: Heat capacity of $SmCrO_3$ as a function of temperature in the range from 150 K to 240 K at a magnetic field of 0 T. **(a)** Shows the heat capacity from [32], **(b)** shows the heat capacity measured in this work. The linear fits show the construction to determine the heat capacity jump at the antiferromagnetic phase transition as described in the text.

[2] The derivative of the susceptibility is multiplied with the applied magnetic field to obtain the magnetisation.

approximation of the local background. The subtraction of a global Debye fit was also performed but proved to be insufficient due to the lacking measurement precision of the heat capacity and the resulting high noise. Note, that the T^3-behavior of phononic background expected at low T does not describe the background at the relatively high T of the SRT. The by the linear background approximation subtracted heat capacity against temperature is shown in Fig. 5.10. A horizontal line emphasizes $c_p = 0$. If the linear background were to approximate the real background perfectly in the vicinity of the phase transition only the anomaly would deviate from this line. However as can be seen the background subtracted heat capacity deviates from the line. The deviation from zero in the vicinity of the anomaly can be split into two contributions. Firstly, a contribution which scatters around a value and exhibits similarities to noise. Secondly a contribution which deviates towards positive values. The first contribution is a consequence of measurement precision. The second contribution shows the limits of the linear approximation of the background. By using eq. 2.11, the entropy change is determined from the heat capacity shown in Fig. 5.10. For the lower and upper boundary of the integral the temperature of the beginning and end of the peak are chosen. The entropy change associated with the SRT is then determined to $\Delta S_{\mathrm{SRT}} = 47(6)\,\mathrm{mJ\,mol^{-1}\,K^{-1}}$. The value agrees with the value of $32(14)\,\mathrm{mJ\,mol^{-1}\,K^{-1}}$ obtained from the magnetisation data at low field parallel to the c axis by means of the Clausius-Clapeyron equation within their uncertainties. In contrast the entropy change determined by the analysis based on the Clausius-Clapeyron equation for the magnetic field parallel to the a axis deviates significantly from the entropy change determined from heat capacity. The entropy change associated with the SRT is determined using the Clausius-Clapeyron equation to $-1.5(14)\,\mathrm{mJ\,mol^{-1}\,K}$. The entropy change deviates from the entropy change determined from heat capacity by $5.4\,\sigma$-intervals. The deviation could be caused by the assumption that a linear extrapolation to 0 T is valid for magnetic fields applied along the a axis. For example it could be that at lower magnetic fields parallel to

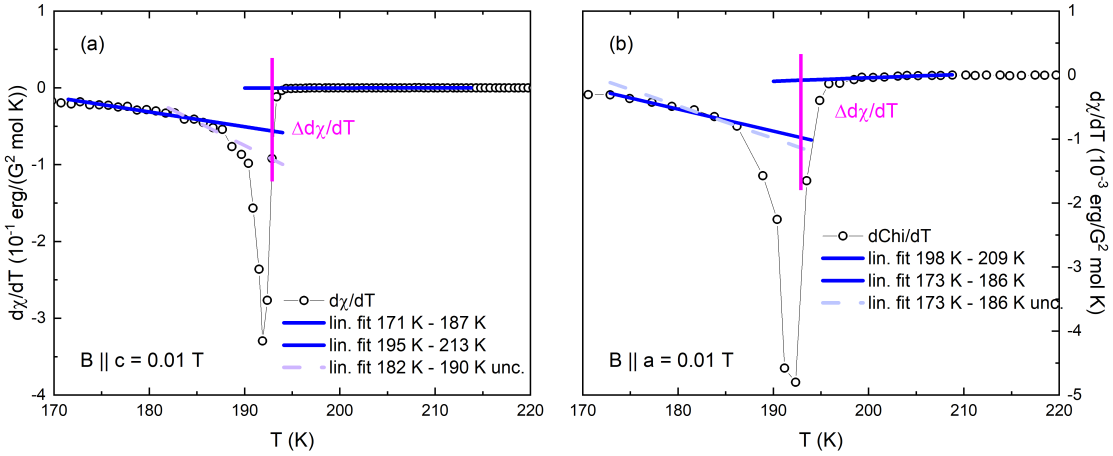


Figure 5.8: $\partial\chi/\partial T$ as a function of temperature with an applied magnetic of 0.01 T along the **(a)** c axis and the **(b)** a axis. The linear fits show the construction that is used to determine the jump at the antiferromagnetic phase transition as described in the text. The data is from [1].

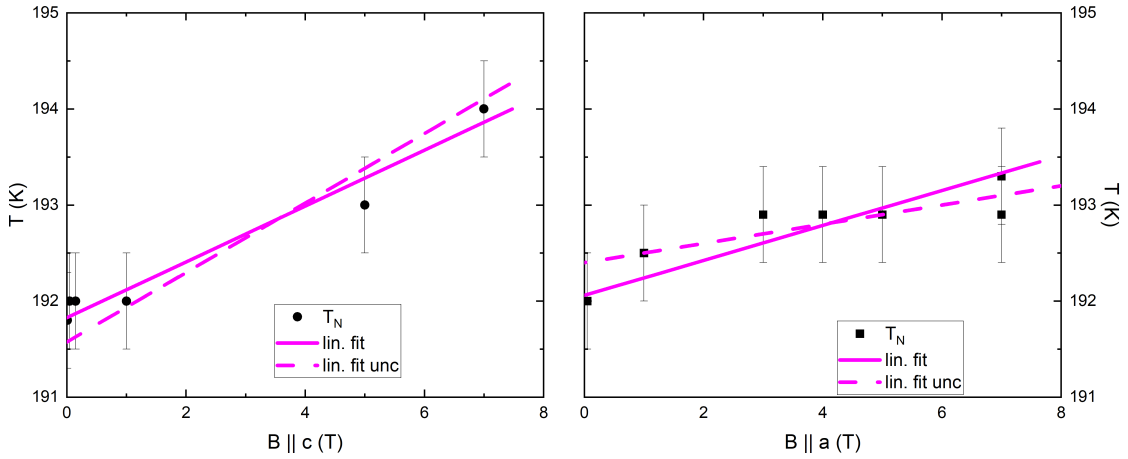


Figure 5.9: The temperature T_N of the antiferromagnetic phase transition as a function of the applied magnetic field in crystallographic **(a)** c and **(b)** a direction. The linear fits are used to determine $\partial T/\partial B$. The data is from [1].

the a axis the entropy change increases with decreasing field.

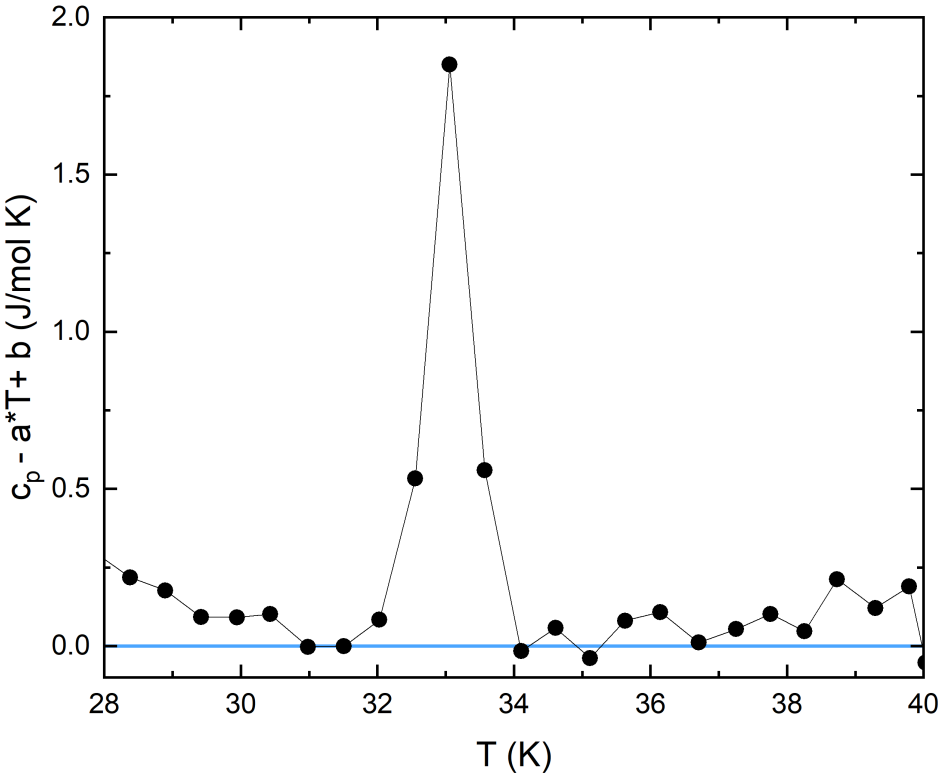


Figure 5.10: Heat capacity corrected by a linear background versus temperature. The background was fitted such that the heat capacity is zero in the vicinity of the peak corresponding to the spin rotation phase transition. The horizontal line indicates where 0 is.

5.2.2 Heat Capacity at B $\neq$ 0 T

For the measurement in applied magnetic fields, a $SmCrO_3$ sample with $m = 0.69(5)$ mg was used. Fig. 5.11 illustrates the heat capacity against temperature measured at various static magnetic fields. All curves show a Debye-like rise and three distinct anomalies, a broad peak at a temperature of 3 K, a dip at 28 K and a peak that occurs at different temperatures depending on the applied magnetic field. The inset shows measurements at 0 T with different sample masses in the range of 25 to 30 K. Here the dip at 28 K is only visible in the measurement with a sample mass of 0.69(5) mg but not in the measurement with a sample mass of 2.41(3) mg. The cause of the dip remains evasive. It could be that the properties of the sample have changed by polishing it. This seems unlikely, as there would need to be an effect contributing a negative heat capacity which amounts to a negative entropy change. The dip could also be a measurement artifact introduced by measuring a sample with a very small mass. But this also seems unlikely as the dip does not appear in an heat capacity measurement conducted on a copper sample with a mass of $m = 0.74$ mg in Fig. 3.5.

The peak of the SRT is shifted towards lower temperatures with increasing magnetic field. This can be explained by the fact, that for increasing fields in crystallographic c direction it becomes energetically favorable for the magnetic moments to remain in the c direction leading to a suppression of the SRT. Furthermore, for each in field measurement, in the temperature range between the temperatures of the in field SRT and the zero field SRT the heat capacity measured in field is lower than in zero field. As temperature increases, the discrepancy between the in-field curves and the zero-field curve diminishes, becoming smaller than the measurement precision above 28 K. Figure 5.12 (a) shows $c_p^{\mathrm{exp}}(B = 14\,\mathrm{T})$, the heat capacity measurement at $B = 14$ T, versus temperature. A Schottky contribution is fitted below a temperature of 5 K. Below 5 K the experimental data are fully explained by the fitted Schottky contribution. Thus the heat capacity is dominated by the Schottky contribution in this temperature regime. Above 5 K the fit lies below the data which signals the contribution of the SRT to the heat capacity. For temperatures above 10 K the measured heat capacity is smaller than the heat capacity that the Schottky peak should contribute. Thus the Schottky peak contributes less to the heat capacity than expected from the fit. To further investigate this the heat capacity of the Schottky anomaly fitted to $c_p^{\mathrm{exp}}(B = 14\,\mathrm{T})$ is added to the in field measurement data above T_{SRT} as shown in Fig. 5.12 (b). Furthermore shown is the zero field measurement and the in field measurement without an added Schottky above T_{SRT} against temperature.

Figure 5.12 (c) shows heat capacity measurements for varying magnetic fields versus temperature. For the in field measurements the contribution of a Schottky anomaly has been added in the same way as for the 14 T measurement curve. The deviation of the in field data from the zero field data is reduced by adding the contribution of the Schottky anomaly. Without the addition of the contribution of the Schottky anomaly the in field curves deviate from the zero field curve up to 28 K. With the

contribution of the Schottky anomaly the in field data deviates from the zero field data up to 21.0(5) K, 16.5(5) K and 16.5(5) K respectively for an applied magnetic field of 7 T, 10 T and 14 T. The in field data agrees with the zero field data at lower temperatures than without the addition of the Schottky contribution. From these observations it is concluded, that the two state system causing the Schottky peak no longer contributes to the heat capacity at temperatures larger than T_{SRT}. This may be caused by a shift in the energy levels, such that either both states or only the ground state are occupied above T_{SRT}.

The evolution of the energy gap of the Schottky anomaly $\Delta_{\mathrm{Schottky}}$ in an external field applied along the c axis is shown in Fig. 5.13. The energy gap rises approximately quadratically with external field, $\Delta_{\mathrm{Schottky}}$ is 9.7(23)% larger at 14 T than at 0 T. As the change of 14 T of the total field causes a 10 % rise, assuming that $\Delta_{\mathrm{Schottky}}$ depends linearly on the external field the internal field acting on the two state system can be very crudely approximated to an order of magnitude of 150 T.

Further investigation of the SRT requires the separation of the SRT peak from the total heat capacity. To seperate the peaks first the fitted Schottky peak was subtracted with the parameters obtained by fitting below 5 K up to the middle of the SRT peak. The exact ending of the Schottky peak in the SRT could not be deter-

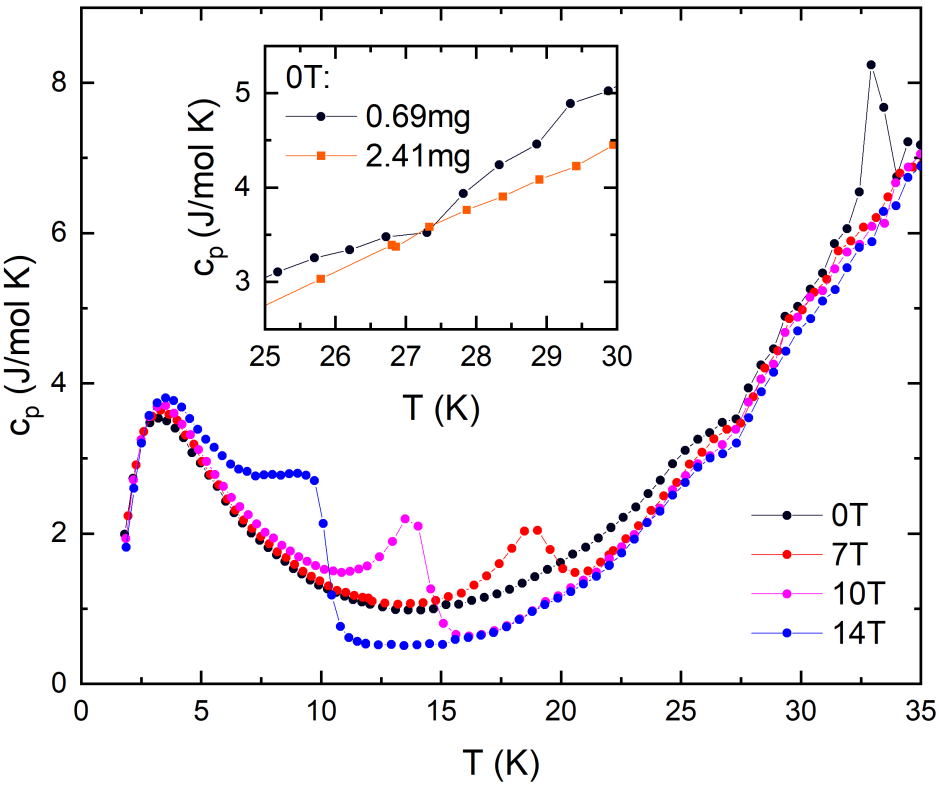


Figure 5.11: Heat capacity versus temperature for various magnetic fields applied along the crystallographic c axis. The measurements in the main plot were performed using a crystal of mass m = 0.69 mg. The inset displays the heat capacity of the sample before and after polishing in the range of 25 K to 30 K.

mined. The end of the Schottky peak at high temperatures is assumed to be abrupt (Heaviside step function like). This assumption leads to a discontinuity which can be seen in the 14 T curve at 10 K. The temperature at which the subtraction of the Schottky peak ends was chosen such that the discontinuity is minimalized. Then a combination of a Debye-Einstein model was fitted at temperatures above the temperature of the SRT and subtracted from the heat capacity. The resulting heat capacities showed negative values for some datasets or the data still showed a background, furthermore some datasets were not measured up to higher temperatures. For the datasets where the subtraction of the background by a Debye-Einstein model was not feasible (4 T, 7 T, 8 T, 11 T, 12 T, 13 T, 14 T), a polynomial of third order was fitted to the data at temperatures above and below in the vicinity of T_{SRT}. The

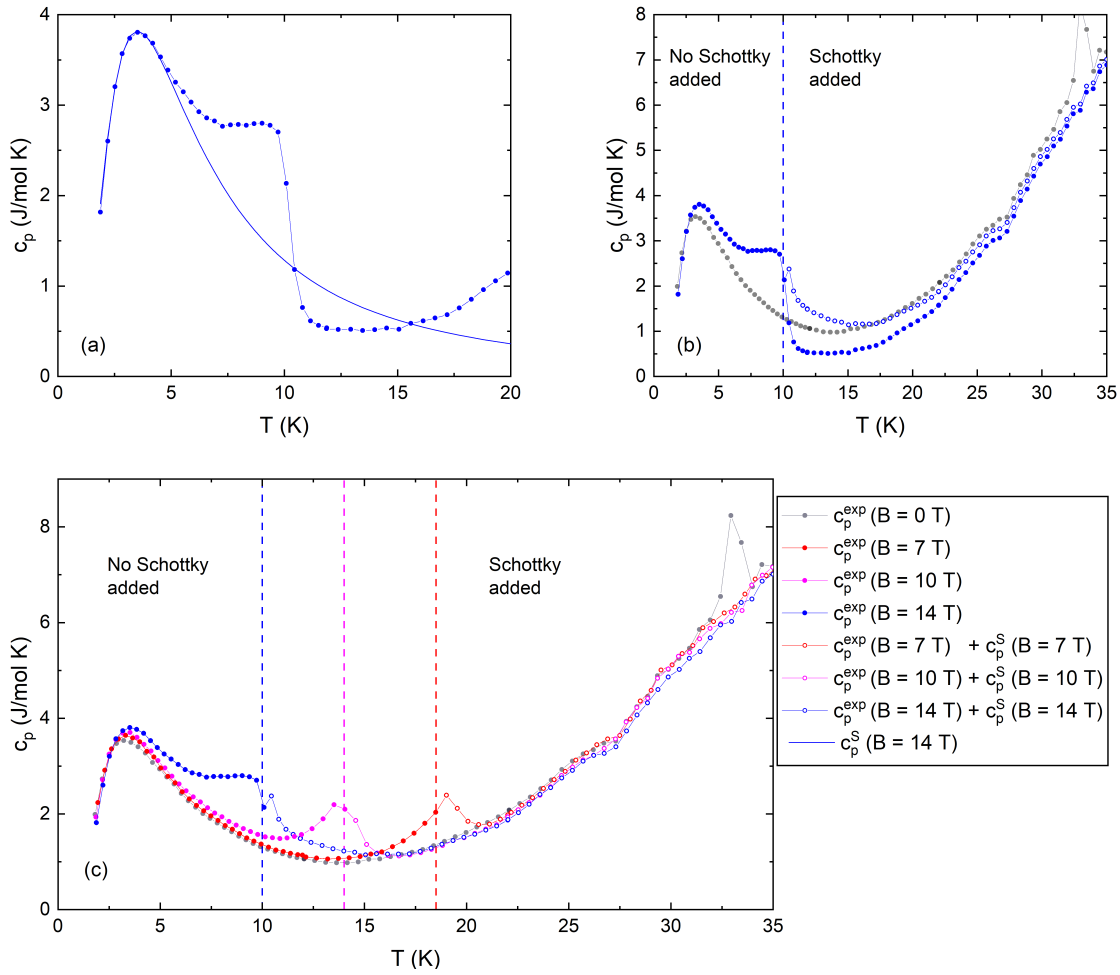


Figure 5.12: Heat capacity measurements against temperature for various magnetic fields. **(a)** Measurement performed at a magnetic field of 14 T and a Schottky anomaly fitted below a temperature of 5 K. **(b)** Measurement performed at a magnetic field of 14 T with the contribution of the Schottky shown in (a) added to the data above 10 K. Grey and blue filled points display the zero field and field measurement. **(c)** Measurements with a applied field of 0, 7, 10 and 14 T. The contributions of the Schottky anomaly fits is added to the data above T_{SRT}.

peak in the zero field curve was determined as discussed in chapter 5.2.1. In Fig. 5.14 the resulting SRT peak is shown for different applied fields in the crystallographic c direction. With increasing magnetic field the peaks become broader in temperature. Starting with 0 T their amplitude first becomes smaller, then larger up to 12 T before they decrease slightly in their maximum again. Furthermore, a second broad small peak can be seen at 7 K for an applied field larger or equal to 8 T. This second feature grows in size with increasing field and is then not discernible anymore from the SRT peak starting at 12 T. The origin of this peak is not known.

The entropy change associated to the SRT peak for varying magnetic fields is calculated using eq. 2.11. The results are compared to the entropy change calculated using the Clausius-Clapeyron equation (eq. 2.5). Figure 5.15 (a) shows the resulting entropy changes versus the applied magnetic field in crystallographic c direction of the SRT. The rise of the entropy change for increasing magnetic fields up to 8 T, determined from the heat capacity measurements, is linear. At larger fields between 10 T and 14 T is a second interval where the entropy change rises linearly but with a larger slope than at lower fields. The increase of the slope of the entropy change

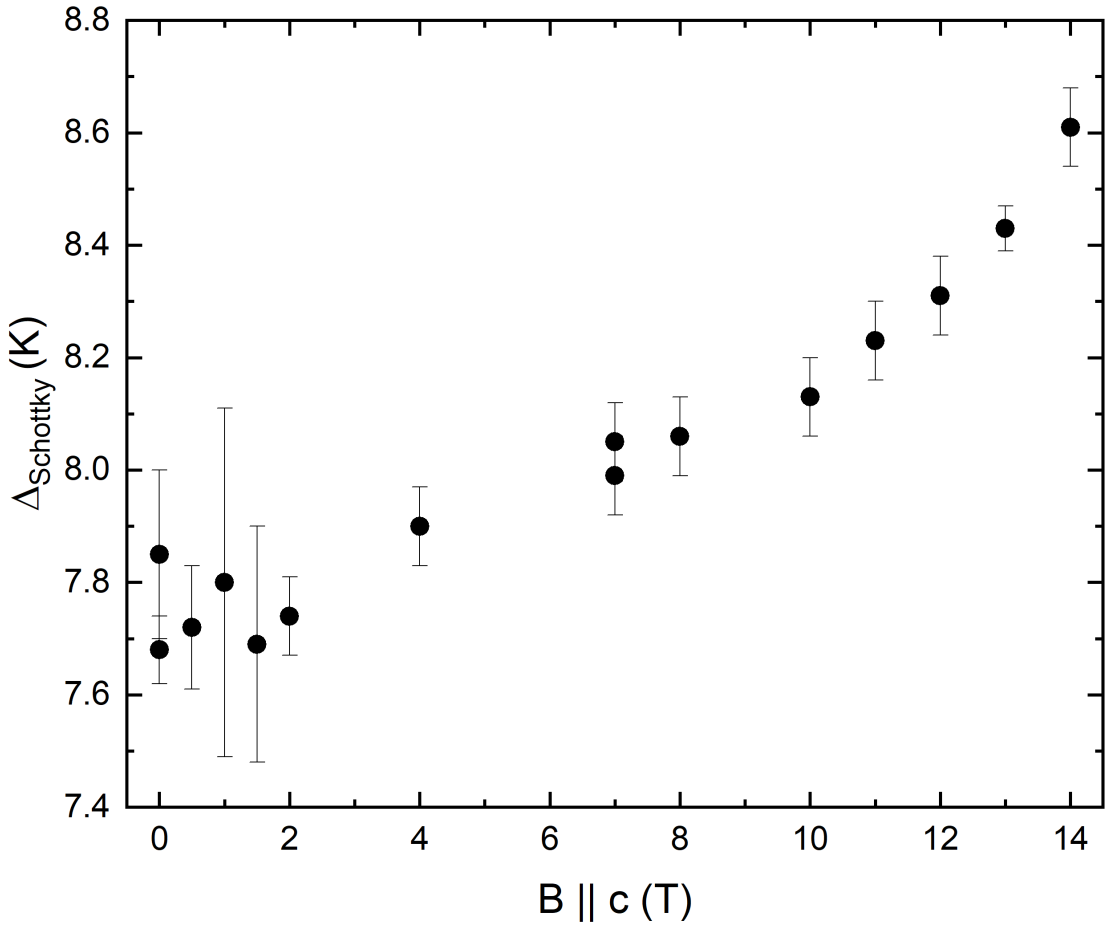


Figure 5.13: Energy gap of the Schottky anomaly in kelvin as a function of magnetic field applied in the crystallographic c direction.

from the linear regime at low fields to that at high fields may be caused by the afore mentioned broad peak. As it starts to merge with the SRT peak at 10 T and grows with magnetic field it cannot be determined and separated at fields above 10 T and could thus contribute to the calculated entropy change. The entropy change determined from the Clausius-Clapeyron equation in Fig. 5.15 (a) lies above the values determined from heat capacity for non zero fields smaller than 10 T. At fields larger or equal to 10 T the values determined with the Clausius-Clapeyron equation are smaller. The entropy change determined from the Clausius-Clapeyron equation is in agreement with the values determined by heat capacity within the measurement uncertainties. However the uncertainties of the entropy changes determined from heat capacity measurements are large. The uncertainties of the entropy changes determined by heat capacity are dominated by the background subtraction. Due to the large errorbars it is not possible to determine wether the entropy change determined from heat capacity is larger or smaller than the one calculated with the Clausius-Clapeyron equation. If the entropy change determined by the Clausius-Clapeyron equation based analysis were significantly larger than the entropy change determined from heat capacity measurements a first order phase transition is extremely unlikely. This would render the validity of the Clausius-Clapeyron equation highly unlikely as a prediction of a to high entropy change would necessitate a negative entropy change contribution for it to still be valid, which would be a very unusual phenomenon. If the entropy change is lower than the entropy change measured in heat capacity there can simply be another contributor to the entropy change. Thus to gain further insights measurements of c_p with a better signal to noise ratio al-

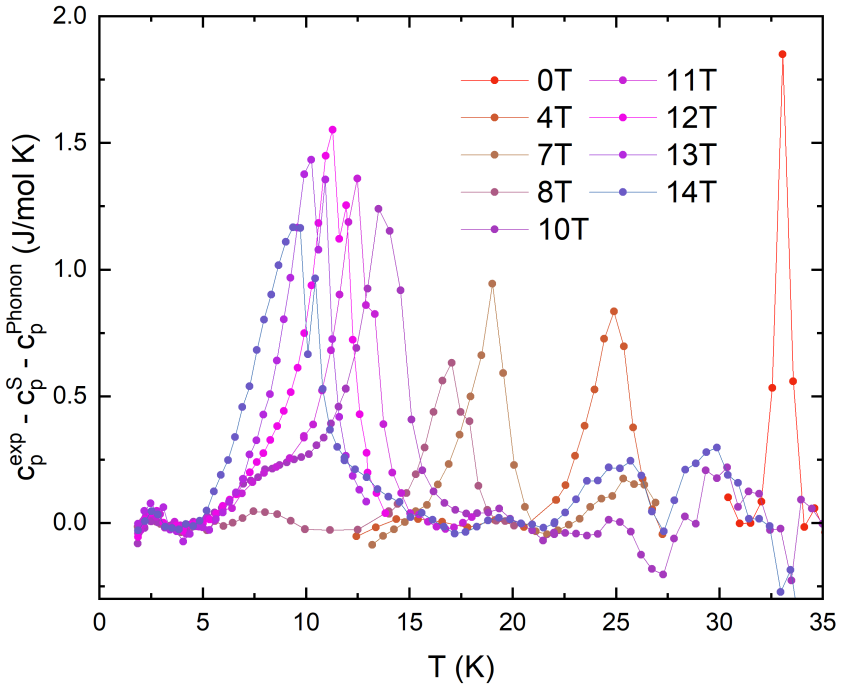


Figure 5.14: Heat capacity associated with the SRT for varying B-fields applied parallel to the crystallographic c direction versus temperature.

lowing a more precise determination of the entropy change associated with the SRT are needed. Low magnetic fields are of particular interest, as the entropy change determined by the Clausius-Clapeyron equation could be significantly higher than that determined by heat capacity measurements in this regime.

A potential contributor to the entropy change at T_{SRT} can be found in the two state system that contributes a Schottky anomaly to the heat capacity. Assuming that the two state system is fully disordered at 35 K above T_{SRT} independently from the applied field it must contribute the same entropy changes when going from the ordered state at 1.8 K to the disordered state at 35 K for all applied fields. This assumes that the two state system is in the same state for 1.8 K and 35 K independently of the applied field. That the two state system is fully disordered independently of the applied field at 35 K seems reasonable, given that the maximum of the Schottky peak occurs within the temperature range of 3.1 to 3.6 K, depending on the field, which is a magnitude lower than the temperature of 35 K. The argument presented in the paragraph above can also be phrased as: The heat capacity that the Schottky anomaly does not contribute above T_{SRT} in field compared to zero field leads to an entropy change $\Delta S_{\mathrm{Schottky}}$ that is not contributed above T_{SRT}. This entropy change must be contributed at other temperatures up to the temperature where the two state system is fully disordered. The entropy change missing in the Schottky peak could be contributed towards the entropy change in the phase transition.

$$\Delta S_{\mathrm{SRT}}(B_1) = \Delta S_{\mathrm{Schottky}}(B_1) + \text{other contributions} \tag{5.3}$$

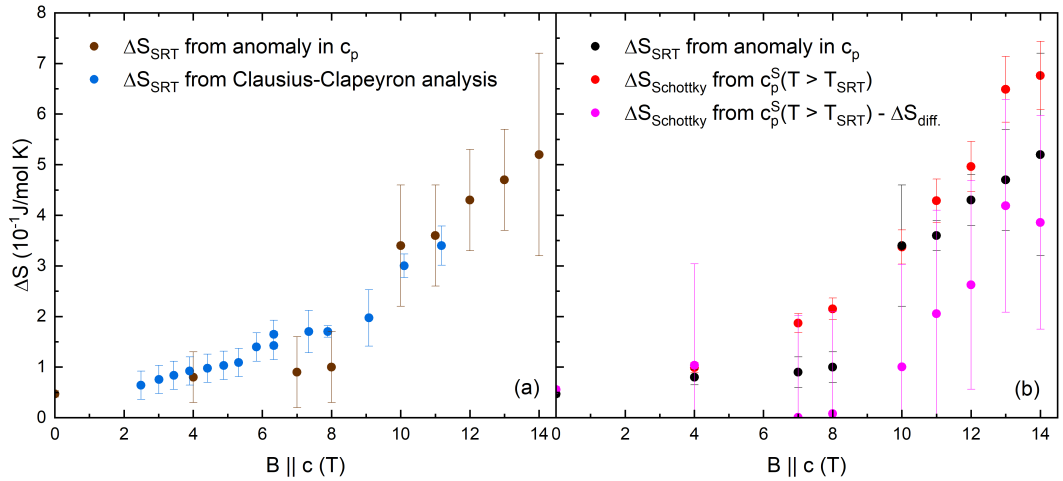


Figure 5.15: Entropy change as a function of the magnetic field in the crystallographic c direction. **(a)** The entropy change (ΔS_{SRT}) associated with the SRT, determined from heat capacity and via the Clausius-Clapeyron analysis, as described in the text. **(b)** ΔS determined by three different methods (described in the text): ΔS_{SRT} is the entropy change determined from heat capacity. $\Delta S_{\mathrm{Schottky}}$ is the entropy change determined from the integral of the Schottky peak in the heat capacity including the data for temperatures above T_{SRT}. ΔS_{diff} is the entropy change calculated by $\Delta S_{\mathrm{diff}} = \Delta S_{\mathrm{Schottky}}(B \neq 0) - \Delta S_{\mathrm{Schottky}}(B = 0)$, as described in the text.

Where $\Delta S_{\mathrm{SRT}}(B_1)$ is the entropy change associated with the SRT in the magnetic field B_1, $\Delta S_{\mathrm{Schottky}}(B_1)$ is the entropy change the Schottky peak would have if it continued above T_{SRT} in the magnetic field B_1. Other contributions are the contributions at the magnetic field B_1 to ΔS_{SRT} by other contributors not identified in this work. Fig. 5.15 (b) shows $\Delta S_{\mathrm{SRT}}(B_1)$ determined from heat capacity measurements and $\Delta S_{\mathrm{Schottky}}(B_1)$ against the magnetic field parallel to the c axis. For the majority of applied magnetic fields they are in agreement within the scope of their uncertainties. However the entropy change the two state system contributes is greater than the entropy change associated with the SRT at all fields except 10 T. This could indicate that the entropy change $\Delta S_{\mathrm{Schottky}}$ is not wholly contributed to ΔS_{SRT}. A part of the entropy change $\Delta S_{\mathrm{Schottky}}$ could also be contributed at temperatures below T_{SRT}. In heat capacity the size of the Schottky peak increases at low fields within the uncertainties for increasing magnetic field, which increases the entropy change contributed by the Schottky peak below T_{SRT} by $\Delta S_{\mathrm{diff.}}$:

$$\Delta S_{\mathrm{diff.}}(B_1) = \Delta S_{\mathrm{Schottky\ T<T_{SRT}}}(B_1) - \Delta S_{\mathrm{Schottky\ T<T_{SRT}}}(B = 0) \tag{5.4}$$

Where $\Delta S_{\mathrm{Schottky\ T<T_{SRT}}}(B_1)$ and $\Delta S_{\mathrm{Schottky\ T<T_{SRT}}}(B = 0)$ are the entropy changes below T_{SRT} of the Schottky anomaly respectively in the magnetic field B_1 and $B = 0$.

The entropy change contributed by the two state system to ΔS_{SRT} is corrected for the increase of contributed entropy change by the Schottky anomaly below T_{SRT} by subtracting $\Delta S_{\mathrm{diff.}}$ from $\Delta S_{\mathrm{Schottky}}$:

$$\Delta S_{\mathrm{SRT}}(B_1) = \Delta S_{\mathrm{Schottky}}(B_1) - \Delta S_{\mathrm{diff.}}(B_1) + \text{other contributions} \tag{5.5}$$

The corrected missing entropy change is shown in Fig. 5.15 (b), it lies below ΔS_{SRT} determined from heat capacity for fields above 4 T, but the datasets agree within the scope of their uncertainties. The uncertainty of the entropy change, that the Schottky anomaly contributes to the entropy change associated with the SRT is increased by the correction due to the uncertainties of the total entropy change of the Schottky fits below T_{SRT}.

5.3 Magnetic Phase Diagrams

Anomalies found in the magnetisation $M(T, B)$ and heat capacity can be used to expand the magnetic phase diagram of $SmCrO_3$, initially constructed in [1]. Fig. 5.16 shows the derivative of isothermal magnetization versus the applied magnetic field in c direction. Data measured at temperatures higher than 20 K and the measurement labeled with 20 K* are taken from [1]. The maxima in the data obtained in [1] and the data obtained in this work are at the same positions as can be seen for the two measurements performed at 20 K. But the linear background and the peak size are different. It is not possible to transform the curves into each other by scaling the data with a factor and adding a constant. The difference might be caused by the polishing of the sample or a imperfect mounting of the sample onto the sample holder causing the magnetic field to not be perfectly parallel to the c axis. The

magnetic field at which the SRT occurs increases with decreasing temperature and the anomaly cannot be detected below 8 K. Fig. 5.17 (a) depicts the derivative of the magnetic susceptibility $\chi = {}^{M}/_{B}$ for different magnetic fields applied along the c axis. At the temperature of 190 K and below 35 K several anomalies can be seen. The inset shows the anomalies below 35 K. The anomalies at 190 K are caused by the antiferromagnetic ordering of the chromium atoms moments. Its temperature is rather constant in field. The anomaly below 35 K is caused by the SRT. With increasing magnetic field the temperatures and amplitudes of the SRT peaks decrease. Fig. 5.17 (b) depicts the derivative of the susceptibility $\chi = {}^{M}/_{B}$ for different magnetic fields along the a axis. At 190 K an anomaly caused by the antiferromagnetic transition with a similar behavior as the anomaly caused by the antiferromagnetic transition in 5.17 (a) can be seen. Below 5 K there is a second anomaly. Its temperature is rather constant in field. The origin of the anomaly is the ordering of the samarium moments [13]. This anomaly can also be seen when the field is applied along the c axis in the heat capacity data.

Using the magnetization measurements shown here a magnetic phase diagram for the field applied along the a and c axis can be determined. For the phase diagram with the magnetic field applied along the c axis the data are supplemented with

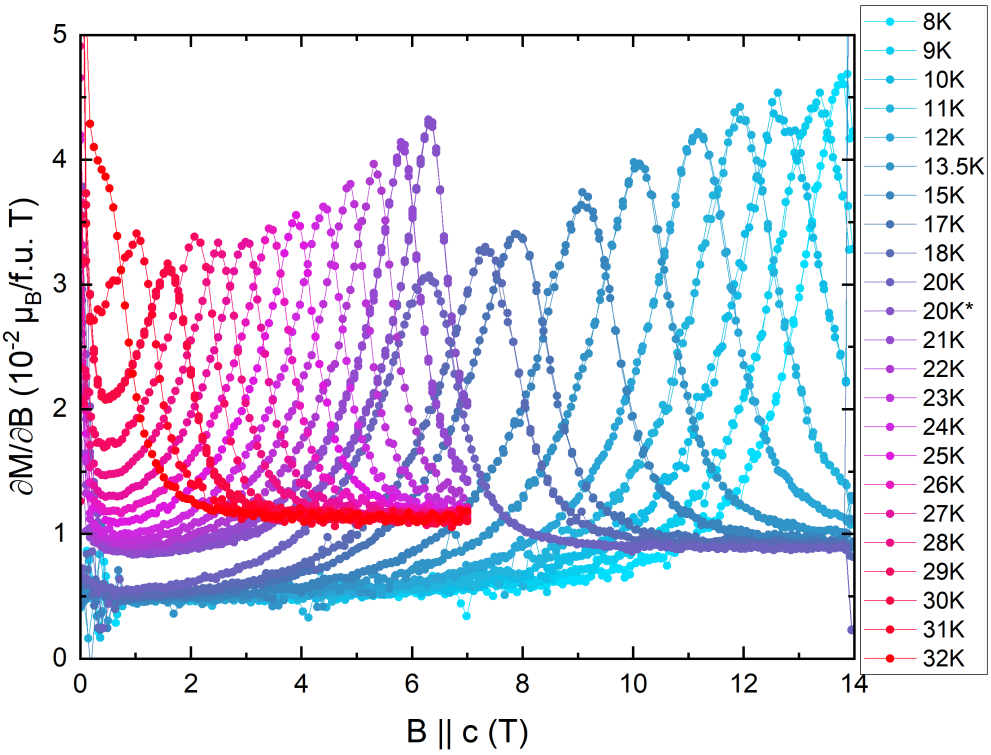


Figure 5.16: The derivative of the isothermal magnetization ${}^{\partial M}/_{\partial B}$ versus the applied Magnetic Field. The data above 20 K and the one marked by * are from [1].

data from heat capacity measurements. In the phase diagram with the magnetic field parallel to the c axis three phases occur and in the phase diagram with the magnetic field parallel to the a axis four phases occur which are explained in chapter 5.1. In the AF III the samarium atoms moments are ordered [13]. Fig. 5.18 (a) shows the phase diagram with the magnetic field applied along the c axis. T_{comp} is the compensation point measured in [1]. It is caused by the antiparallel alignment of the

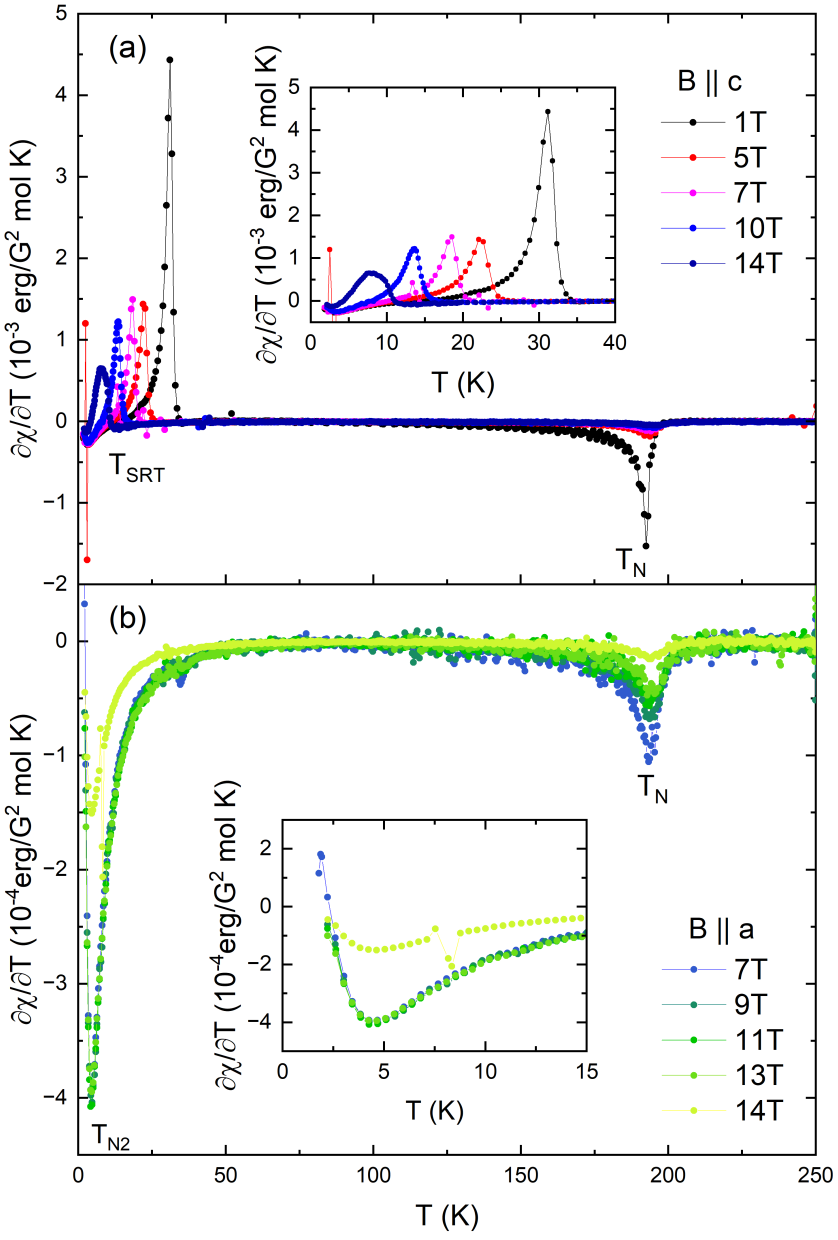


Figure 5.17: Derivative of the magnetic susceptibility $\partial\chi/\partial T$ measured at various applied magnetic fields versus temperature. The magnetization was measured in the field cooled mode. **(a)** Magnetic field applied along the c axis, the curve at 1, 5 and 7 T are from [1]. **(b)** The magnetic field applied along the a axis. The insets depict the anomalies at lower temperature in greater detail.

magnetic moment of chromium atoms and the samarium atoms which compensate each other leading to $\chi = 0$. The antiferromagnetic phase transition shifts only slightly in temperature with increasing magnetic field for magnetic fields applied along the a and c axis. Furthermore the ordering of the samarium atoms moments shifts only slightly in temperature with increasing magnetic field parallel to the a axis. The temperature of the SRT drops linear with increasing magnetic field. To higher magnetic fields the value of the slope increases which can be seen in Fig. 5.4 (b). Above a magnetic field of 10 T, T_{SRT} determined from the heat capacity is larger than that determined from magnetisation measurements. The difference in temperature has a size of 1.7 K. The cause is probably that the temperature at which the heat capacity change is strongest is not the temperature at which the change in magnetisation has its maximum. As the width of the peak of the SRT increases in field (Fig. 5.17 (a) inset) and heat capacity (Fig. 5.14) the determined temperatures can also lie further apart in the temperature range at which the SRT takes place. The magnetic phase diagram with a magnetic field applied along the a-direction is shown in Fig. 5.18 (b). The Γ_2 configuration with the resulting magnetic moment of the chromium atoms along the a axis extends up to the paramagnetic phase. The anti-ferromagnetism with the resulting chromium moments along the c axis is inside a dome.

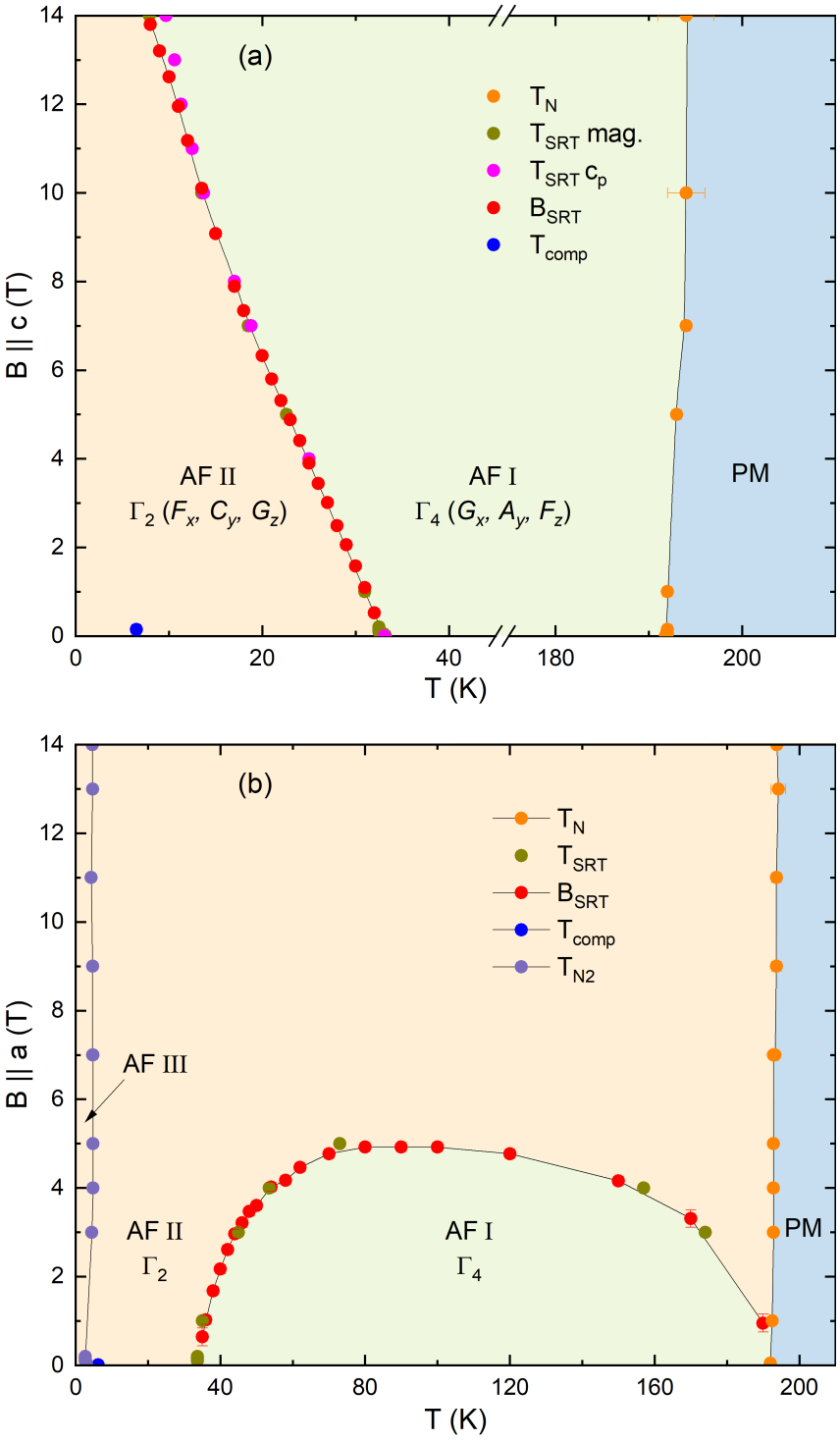


Figure 5.18: Magnetic phase diagrams of $SmCrO_3$ for an applied B-field in the crystallographic **(a)** c direction and **(b)** a direction. PM is the paramagnetic phase. In the AF I phase the Cr moments order in an antiferromagnetic configuration with the resulting moment of the Cr atoms along the c axis (Γ_4 configuration). In the antiferromagnetic AF II phase the resulting moment of the Cr atoms are aligned along the a axis (Γ_2 configuration). The Cr moments do not change from the AF II phase to the AF III phase but the Sm^{3+} moments may order in the AF III phase. Data below 7 T with the exception of T_{SRT} c_p is from [1].

Chapter 6

Conclusions

For the present work heat capacity and magnetisation measurements on $SmCrO_3$ and thermal expansion and magnetostriction measurements on Fe_3GeTe_2 were conducted. The heat capacity is measured using a relaxation method whilst thermal expansion and magnetostriction are determined using capacitive dilatometry. These methods access a temperature regime that spans from 1.8 K to 300 K with applied magnetic fields from 0 T to 15 T for measuring with capacitive dilatometry and from 0 T to 14 T for measuring heat capacity.

Dilatometric measurements on the 2D Van-der-Waals material Fe_3GeTe_2 were performed along the c axis. The thermal expansion coefficient shows a broad anomaly including a narrow peak. The overall feature can be assigned to the ferromagnetic phase transition, showing that there is magnetoelastic coupling in Fe_3GeTe_2. The shape of the ferromagnetic phase transition in thermal expansion differs from that seen in heat capacity measurements [39]. The magnetostriction data show a expansion of the material up to a kink at 0.4 T, which is caused by the magnetic moments aligning with the field. At higher magnetic fields the kink is followed by a large hysteresis between up and down sweep of the magnetic field. The origin of the hysteresis remains elusive.

Heat capacity measurements on $SmCrO_3$ feature a Schottky anomaly, an anomaly at the spin rotation transition and an anomaly at the antiferromagnetic phase transition. The entropy change associated with the spin rotation transition in zero field is determined to $0.047(6)\,\mathrm{J\,mol^{-1}\,K^{-1}}$ from heat capacity measurements. It is in good agreement to the entropy change of $0.032(14)\,\mathrm{J\,mol^{-1}\,K^{-1}}$ determined from magnetisation measurements along the c axis. However it deviates significantly from the entropy change of $-0.0015(14)\,\mathrm{J\,mol^{-1}\,K^{-1}}$ determined from magnetisation measurements along the a axis. The deviation is probably caused by the too simple approximation of the entropy change to $B = 0\,\mathrm{T}$ by a linear function. The Schottky anomaly is not observable when measuring in an applied magnetic field in the Γ_4 configuration. Thus the Schottky anomaly does not contribute to the heat capacity measured in field above T_{SRT} where the chromium magnetic moments order is described by the Γ_4 configuration

The entropy changes associated with the spin rotation transition are determined for magnetic fields up to 14 T and compared to the entropy changes calculated using the Clausius-Clapeyron equation. The values agree within their uncertainties. The suppressed ordering of the Schottky anomaly in the Γ_4 configuration is identified as a contributor to the entropy changes of the spin rotation transition. Furthermore the magnetic phase diagrams in [1] are continued up to magnetic fields of 14 T.

Bibliography

[1] N. Yuan. *High-Pressure Single Crystal Growth and Magnetization Studies on Correlated Electron Systems*. 2024.

[2] C. M. Alan Menken Tim Rice. *A Whole New World*. 1992.

[3] Z. Fei, B. Huang, P. Malinowski, W. Wang, T. Song, J. Sanchez, W. Yao, D. Xiao, X. Zhu, A. F. May, et al. Two-dimensional itinerant ferromagnetism in atomically thin Fe3GeTe2. *Nature materials*, 17(9):778–782, 2018.

[4] N. D. Mermin and H. Wagner. Absence of Ferromagnetism or Antiferromagnetism in One- or Two-Dimensional Isotropic Heisenberg Models. *Phys. Rev. Lett.*, 17:1133–1136, 22 Nov. 1966.

[5] Y. Deng, Y. Yu, Y. Song, J. Zhang, N. Z. Wang, Z. Sun, Y. Yi, Y. Z. Wu, S. Wu, J. Zhu, et al. Gate-tunable room-temperature ferromagnetism in two-dimensional Fe3GeTe2. *Nature*, 563(7729):94–99, 2018.

[6] K. S. Burch, D. Mandrus, and J.-G. Park. Magnetism in two-dimensional van der Waals materials. *Nature*, 563(7729):47–52, 2018.

[7] R. Küchler, A. Wörl, P. Gegenwart, M. Berben, B. Bryant, and S. Wiedmann. The world's smallest capacitive dilatometer, for high-resolution thermal expansion and magnetostriction in high magnetic fields. *Review of Scientific Instruments*, 88(8):083903, Aug. 2017. ISSN: 0034-6748. eprint: `https://pubs.aip.org/aip/rsi/article-pdf/doi/10.1063/1.4997073/13527622/083903\_1\_online.pdf`.

[8] M. Zhu, Y. You, G. Xu, J. Tang, Y. Gong, and F. Xu. Strain modulation of magnetic coupling in the metallic van der waals magnet Fe3GeTe2. *Intermetallics*, 131:107085, 2021. ISSN: 0966-9795.

[9] R. Hornreich. Magnetic interactions and weak ferromagnetism in the rare-earth orthochromites. *Journal of Magnetism and Magnetic Materials*, 7(1):280–285, 1978. ISSN: 0304-8853.

[10] T. Yamaguchi. Theory of spin reorientation in rare-earth orthochromites and orthoferrites. *Journal of Physics and Chemistry of Solids*, 35(4):479–500, 1974. ISSN: 0022-3697.

[11] X. Qian, L. Chen, S. Cao, and J. Zhang. A study of the spin reorientation with t–e orbital hybridization in SmCrO3. *Solid State Communications*, 195:21–25, 2014. ISSN: 0038-1098.

[12] M. Tripathi, R. J. Choudhary, D. M. Phase, T. Chatterji, and H. E. Fischer. Evolution of magnetic phases in $SmCrO_3$: A neutron diffraction and magnetometric study. *Phys. Rev. B*, 96:174421, 17 Nov. 2017.

[13] T. Sau, P. Yadav, S. Sharma, R. Raghunathan, P. Manuel, V. Petricek, U. P. Deshpande, and N. P. Lalla. High-resolution time of flight neutron diffraction and magnetization studies of spin reorientation and polar transitions in $SmCrO_3$. *Phys. Rev. B*, 103:144418, 14 Apr. 2021.

[14] T. Sau, S. Sharma, P. Yadav, R. Baumbach, T. Siegrist, A. Banerjee, and N. P. Lalla. First-order nature of the spin-reorientation phase transition in $SmCrO_3$. *Phys. Rev. B*, 106:064413, 6 Aug. 2022.

[15] M. El Amrani, M. Zaghrioui, V. Ta Phuoc, F. Gervais, and N. E. Massa. Local symmetry breaking and spin–phonon coupling in SmCrO3 orthochromite. *Journal of Magnetism and Magnetic Materials*, 361:1–6, 2014. ISSN: 0304-8853.

[16] Z. Xiang, J. Xu, Y. Huang, S. Ge, and Y. Cui. Novel multiferroicity in orthorhombic SmCrO3. *Progress in Natural Science: Materials International*, 28(5):609–613, 2018. ISSN: 1002-0071.

[17] F. Schwabl. *Statistische Mechanik. mit 26 Tabellen und 186 Aufgaben*. ger. 2., aktualisierte Aufl. Physics and astronomy online library. Berlin ; Heidelberg [u.a.]: Springer, 2004, XVIII, 589 S. ISBN: 3-540-20360-5.

[18] N. W. Ashcroft and N. D. Mermin. *Festkörperphysik*. ger. 4., verbesserte Auflage. Für Bachelor- und Masterstudenten der Physik. München: Oldenbourg Verlag, 2013, XXX, 1050 Seiten. ISBN: 978-3-486-71301-5.

[19] S. Blundell. *Magnetism in condensed matter*. eng. Oxford master series in condensed matter physics. Includes bibliographical references and index. - Description based on print version record. Oxford ; New York: Oxford University Press, 2001, Online Ressource (XII, 238 S.) ISBN: 0-585-48360-4.

[20] S. Blundell and K. M. Blundell. *Concepts in thermal physics*. eng. 2nd edition. Literaturverzeichnis: Seiten 485-487 ; Hier auch später erschienene, unveränderte Nachdrucke. Oxford ; New York ; Auckland ; Cape Town ; Dar es Salaam ; Hong Kong: Oxford University Press, 2010, xviii, 493 Seiten. ISBN: 978-0-19-956209-1.

[21] L. M. Gries. *Experimentelle Untersuchung der Ilmenit-Titanate MnTiO3 und Mn0.75Ni0.25TiO3 mittels hochauflösender Kapazitätsdilatometrie*. Nov. 2021.

[22] T. Barron and G. White. *Heat Capacity and Thermal Expansion at Low Temperatures*. Springer New York, NY, 1999. ISBN: 978-0-306-46198-9.

[23] R. Gross and A. Marx. *Festkörperphysik*. ger. 4., aktualisierte Auflage. De Gruyter Studium. Berlin ; Boston: De Gruyter, 2023, 1 Online–Ressource (XIX, 1067 Seiten). ISBN: 978-3-11-078264-6.

[24] E. Grüneisen. Theorie des festen Zustandes einatomiger Elemente. *Annalen der Physik*, 344(12):257–306, 1912. eprint: `https://onlinelibrary.wiley.com/doi/pdf/10.1002/andp.19123441202`.

[25] T. Kleinbek. *Thermodynamic and magnetic studies on the quantum spin liquid candidate systems Sr3CuSb2O9, Sr3ZnIr2O9 and Sr3CuIr2O9*. 2024.

[26] A. Tari. *The specific heat of matter at low temperatures*. World Scientific, 2003.

[27] Q. Design. *Physical Property Measurement System, Heat Capacity Option User's Manual*. 27th ed. 2017.

[28] Q. Design. *Physical Property Measurement System Cryopump High-Vacuum Option User's Manual*. 3rd ed. 2004.

[29] A. Elghandour. *Thermodynamic and Magnetic Studies on Correlated Electron Systems with Competing Interactions*. 2023.

[30] G. K. White and S. J. Collocott. Heat Capacity of Reference Materials: Cu and W. *Journal of Physical and Chemical Reference Data*, 13(4):1251–1257, Oct. 1984. ISSN: 0047-2689. eprint: https://pubs.aip.org/aip/jpr/article-pdf/13/4/1251/9766222/1251_1_online.pdf.

[31] R. Stevens and J. Boerio-Goates. Heat capacity of copper on the ITS-90 temperature scale using adiabatic calorimetry. *The Journal of Chemical Thermodynamics*, 36(10):857–863, 2004. ISSN: 0021-9614.

[32] P. Gupta and P. Poddar. Study of magnetic and thermal properties of SmCrO3 polycrystallites. *RSC Adv.*, 6:82014–82023, 85 2016.

[33] R. Küchler, R. Wawrzyńczak, H. Dawczak-Dębicki, J. Gooth, and S. Galeski. New applications for the world's smallest high-precision capacitance dilatometer and its stress-implementing counterpart. *Review of Scientific Instruments*, 94(4):045108, Apr. 2023. ISSN: 0034-6748. eprint: https://pubs.aip.org/aip/rsi/article-pdf/doi/10.1063/5.0141974/16833462/045108_1_5.0141974.pdf.

[34] S. Sprachmann. *Thermal Expansion and Magnetostriction of Layered Correlated Electron Systems*. 2021.

[35] R. Küchler, T. Bauer, M. Brando, and F. Steglich. A compact and miniaturized high resolution capacitance dilatometer for measuring thermal expansion and magnetostriction. *Review of Scientific Instruments*, 83(9):095102, Sept. 2012. ISSN: 0034-6748. eprint: https://pubs.aip.org/aip/rsi/article-pdf/doi/10.1063/1.4748864/15675388/095102_1_online.pdf.

[36] F. R. Kroeger and C. A. Swenson. Absolute linear thermal-expansion measurements on copper and aluminum from 5 to 320 K. *Journal of Applied Physics*, 48(3):853–864, Mar. 1977. ISSN: 0021-8979. eprint: https://pubs.aip.org/aip/jap/article-pdf/48/3/853/18375930/853_1_online.pdf.

[37] R. Küchler. personal communication. 2024.

[38] I. Quantum Design. *Magnetic Property Measurement System MPMS3 User's Manual*. 15th ed. June 2016.

[39] R. K. Kremer and E. Brücher. Thermal and magnetoelastic properties of the van der Waals ferromagnet $Fe_{3-\delta}GeTe_2$: Anisotropic spontaneous magnetostriction and ferromagnetic magnon excitations. *Phys. Rev. Mater.*, 8:024002, 2 Feb. 2024.

[40] B. Liu, Y. Zou, S. Zhou, L. Zhang, Z. Wang, H. Li, Z. Qu, and Y. Zhang. Critical behavior of the van der Waals bonded high TC ferromagnet Fe3GeTe2. *Scientific Reports*, 7(1):6184, 2017.

[41] D. J. O'Hara, Z. E. Brubaker, R. L. Stillwell, E. F. O'Bannon, A. A. Baker, D. Weber, L. B. B. Aji, J. E. Goldberger, R. K. Kawakami, R. J. Zieve, J. R. Jeffries, and S. K. McCall. Suppression of magnetic ordering in Fe-deficient $Fe_{3-x}GeTe_2$ from application of pressure. *Phys. Rev. B*, 102:054405, 5 Aug. 2020.

[42] Y. Wang, C. Wang, S.-J. Liang, Z. Ma, K. Xu, X. Liu, L. Zhang, A. S. Admasu, S.-W. Cheong, L. Wang, M. Chen, Z. Liu, B. Cheng, W. Ji, and F. Miao. Strain-Sensitive Magnetization Reversal of a van der Waals Magnet. *Advanced Materials*, 32(42):2004533, 2020. eprint: `https://onlinelibrary.wiley.com/doi/pdf/10.1002/adma.202004533`.

[43] N.-T. Dang, D. P. Kozlenko, O. N. Lis, S. E. Kichanov, Y. V. Lukin, N. O. Golosova, B. N. Savenko, D.-L. Duong, T.-L. Phan, T.-A. Tran, and M.-H. Phan. High Pressure-Driven Magnetic Disorder and Structural Transformation in Fe3GeTe2: Emergence of a Magnetic Quantum Critical Point. *Advanced Science*, 10(9):2206842, 2023. eprint: `https://onlinelibrary.wiley.com/doi/pdf/10.1002/advs.202206842`.

[44] H.-J. Deiseroth, K. Aleksandrov, C. Reiner, L. Kienle, and R. K. Kremer. Fe3GeTe2 and Ni3GeTe2 – Two New Layered Transition-Metal Compounds: Crystal Structures, HRTEM Investigations, and Magnetic and Electrical Properties. *European Journal of Inorganic Chemistry*, 2006(8):1561–1567, 2006. eprint: `https://chemistry-europe.onlinelibrary.wiley.com/doi/pdf/10.1002/ejic.200501020`.

[45] M. Sablik and D. Jiles. Coupled magnetoelastic theory of magnetic and magnetostrictive hysteresis. *IEEE Transactions on Magnetics*, 29(4):2113–2123, 1993.

[46] K. Momma and F. Izumi. *VESTA3* for three-dimensional visualization of crystal, volumetric and morphology data. *Journal of Applied Crystallography*, 44(6):1272–1276, Dec. 2011.

[47] J. Prado-Gonjal, R. Schmidt, J.-J. Romero, D. Ávila, U. Amador, and E. Morán. Microwave-assisted synthesis, microstructure, and physical properties of rare-earth chromites. *Inorganic chemistry*, 52(1):313–320, 2013.

[48] X. Qian, L. Chen, S. Cao, and J. Zhang. A study of the spin reorientation with t–e orbital hybridization in SmCrO3. *Solid State Communications*, 195:21–25, 2014. ISSN: 0038-1098.

[49] M. Tripathi, R. J. Choudhary, and D. M. Phase. Phase coexistence and the magnetic glass-like phase associated with the Morin type spin reorientation phase transition in SmCrO3. *RSC Adv.*, 6:90255–90262, 93 2016.

[50] B. Rajeswaran, D. I. Khomskii, A. K. Zvezdin, C. N. R. Rao, and A. Sundaresan. Field-induced polar order at the Néel temperature of chromium in rare-earth orthochromites: Interplay of rare-earth and Cr magnetism. *Phys. Rev. B*, 86:214409, 21 Dec. 2012.

[51] R. L. White. Review of Recent Work on the Magnetic and Spectroscopic Properties of the Rare-Earth Orthoferrites. *Journal of Applied Physics*, 40(3):1061–1069, Mar. 1969. ISSN: 0021-8979. eprint: `https://pubs.aip.org/aip/jap/article-pdf/40/3/1061/18349238/1061\_1\_online.pdf`.

[52] R. Klingeler. *Spin und Ladungsordnung in Übergangsmetalloxiden, Thermodynamische und magnetische Untersuchungen*. 2003. ISBN: 3-89820-553-3.

[53] H. Stanley. *Introduction to Phase Transitions and Critical Phenomena*. International series of monographs on physics. Oxford University Press, 1987. ISBN: 9780195053166.

Note of gratitude

Many people have accompanied and led me on the journey of my master thesis and to my master thesis.

Firstly, I want to thank Prof. Dr. Rüdiger Klingeler for the opportunity to write my master thesis in his research group. I also thank him for many discussions about the data measured bringing light into the dark and finding solutions when I did not see any if something did not work. Furthermore I am grateful for him taking me to the AGYA conference where I met many nice people and for having fueled my interest in correlated electron systems in lectures before my master thesis.

Secondly, I want to thank Prof. Dr. Christian Enss for taking the role as second referee for this thesis.

I want to thank all current and former people in the F25 group. Especially Lukas Gries who supervised me, showed me the experimental and theoretical methods of dilatometric measurements, an unfortunate amount of Cryo fixing while being fun to be around. Furthermore I am very grateful that he proof read the first version of my master thesis making it readable. I would like to express my sincere gratitude to Ahmed Elghandour who gave me a great deal of knowledge on the working of the PPMS and how to measure heat capacity and for correcting parts of my thesis. I want to thank the many people in the group who made being at the institute fun such as Marius who shared an office with me.

I wish to thank Ning Yuan who provided the $SmCrO_3$ sample and whom I could always ask when I had questions concerning the material. I also thank Reinhard Kremer and Eva Brüchner for providing the Fe_3GeTe_2 samples.

I also want to thank my family for having my back, even when I had doubts. I am particularly grateful that my parents encouraged and awakened my interest in nature. But also for bringing me back down to earth when I needed it and everything else which is too long to write down here.

Lastly I want to thank Birte who always had the time to discuss physics with me and accompanied me during my physic studies. It is fun to explore physics with you and the questions you came up with always lead to great discussions deepening my understanding of physics.

Declaration

I declare that I have written this thesis independently and have not used any sources and aids other than those indicated.

Heidelberg, June 6, 2024
Erik Walendy

